

The Simons Observatory: Assessing the Impact of Dust Complexity on the Recovery of Primordial B -modes

YIQI LIU,¹ SUSANNA AZZONI,¹ SUSAN E. CLARK,^{2,3} BRANDON S. HENSLEY,⁴ LÉO VACHER,⁵ DAVID ALONSO,⁶
CARLO BACCIGALUPI,^{5,7,8} MICHAEL L. BROWN,⁹ ALESSANDRO CARONES,⁵ JENS CHLUBA,⁹ JO DUNKLEY,^{1,10}
CARLOS HERVÍAS-CAIMAPO,¹¹ BRADLEY R. JOHNSON,¹² NICOLETTA KRACHMALNICOFF,^{5,7,8} GIUSEPPE PUGLISI,^{13,14,15}
MATHIEU REMAZEILLES,¹⁶ AND KEVIN WOLZ⁶

¹*Department of Physics, Princeton University, Jadwin Hall, Princeton, NJ 08544, USA*

²*Department of Physics, Stanford University, Stanford, CA 94305, USA*

³*Kavli Institute for Particle Astrophysics & Cosmology, P.O. Box 2450, Stanford University, Stanford, CA 94305, USA*

⁴*Jet Propulsion Laboratory, California Institute of Technology, 4800 Oak Grove Drive, Pasadena, CA 91109, USA*

⁵*The International School for Advanced Studies (SISSA), via Bonomea 265, I-34136 Trieste, Italy*

⁶*Department of Physics, University of Oxford, Denys Wilkinson Building, Keble Road, Oxford OX1 3RH, United Kingdom*

⁷*The National Institute for Nuclear Physics (INFN), via Valerio 2, I-34127, Trieste, Italy*

⁸*The Institute for Fundamental Physics of the Universe (IFPU), Via Beirut 2, I-34151, Trieste, Italy*

⁹*Jodrell Bank Centre for Astrophysics, Department of Physics and Astronomy, Alan Turing Building, The University of Manchester, Manchester M13 9PL, United Kingdom*

¹⁰*Department of Astrophysical Sciences, Princeton University, Peyton Hall, Princeton, NJ 08544, USA*

¹¹*Instituto de Astrofísica and Centro de Astro-Ingeniería, Facultad de Física, Pontificia Universidad Católica de Chile, Av. Vicuña Mackenna 4860, 7820436 Macul, Santiago, Chile*

¹²*Department of Astronomy, University of Virginia, Charlottesville, VA 22904, USA*

¹³*Dipartimento di Fisica e Astronomia, Università degli Studi di Catania, via S. Sofia, 64, 95123, Catania, Italy*

¹⁴*The National Institute for Nuclear Physics (INFN) - Sezione di Catania, Via S. Sofia 64, 95123 Catania, Italy*

¹⁵*INAF - Osservatorio Astrofisico di Catania, via S. Sofia 78, 95123 Catania, Italy*

¹⁶*Instituto de Física de Cantabria (CSIC-UC), Avenida de los Castros s/n, 39005 Santander, Spain*

ABSTRACT

We investigate how dust foreground complexity can affect measurements of the tensor-to-scalar ratio, r , in the context of the Simons Observatory, using a cross-spectrum component separation analysis. Employing a suite of simulations with realistic Galactic dust emission, we find that spatial variation in the dust frequency spectrum, parametrized by β_d , can bias the estimate for r when modeled using a low-order moment expansion to capture this spatial variation. While this approach performs well across a broad range of dust complexity, the bias increases with more extreme spatial variation in dust frequency spectrum, reaching as high as $r \sim 0.03$ for simulations with no primordial tensors and a spatial dispersion of $\sigma(\beta_d) \simeq 0.3$ —the most extreme case considered, yet still consistent with current observational constraints. This bias is driven by changes in the ℓ -dependence of the dust power spectrum as a function of frequency that can mimic a primordial B -mode tensor signal. Although low-order moment expansions fail to capture the full effect when the spatial variations of β_d become large and highly non-Gaussian, our results show that extended parametric methods can still recover unbiased estimates of r under a wide range of dust complexities. We further find that the bias in r , at the highest degrees of dust complexity, is largely insensitive to the spatial structure of the dust amplitude and is instead dominated by spatial correlations between β_d and dust amplitude, particularly at higher orders. If β_d does spatially vary at the highest levels investigated here, we would expect to use more flexible foreground models to achieve an unbiased constraint on r for the noise levels anticipated from the Simons Observatory.

Keywords: Cosmology (343), Cosmic inflation (319), CMB (322), Diffuse radiation (383)

1. INTRODUCTION

A detection of primordial gravitational waves (PGWs) through their imprint on the polarization of the cos-

mic microwave background (CMB) would offer a powerful probe of the physics of the early Universe. PGWs arise as tensor perturbations of the metric and generate a parity-odd polarization pattern in the CMB, known as the primordial B -mode, via Thomson scattering of anisotropic radiation off free electrons at recombination and reionization (Kamionkowski et al. 1997; Seljak & Zaldarriaga 1997). The amplitude of the primordial tensor perturbations compared to the primordial density perturbations is parametrized as the tensor-to-scalar ratio, r . Tensor perturbations are a generic prediction of inflationary models, produced during a period of rapid expansion in the early Universe (Guth 1981; Linde 1982), and their amplitude directly relates to the energy scale of inflation. Constraints from the joint analysis of BICEP/Keck, WMAP, and Planck data limit $r < 0.032 - 0.036$ at the 95% confidence level (BICEP/Keck Collaboration et al. 2021; Tristram et al. 2022).

Targeting this signal has motivated the design of a new generation of CMB polarization experiments, both ground-based and space-borne, that aim to survey the polarized microwave sky with unprecedented sensitivity and frequency coverage over the coming decade. Several of these, such as the BICEP/Keck Array, the Simons Observatory (SO), and CMB-S4, will focus on detecting degree-scale B -modes associated with the “recombination bump” in the CMB power spectrum around $\ell \sim 100$ (Ade et al. 2019, 2022; Abazajian et al. 2022). While ground-based observations are limited by atmospheric noise on the largest angular scales, they will be highly sensitive at intermediate scales. In parallel, the future *LiteBIRD* satellite mission is expected to target both the recombination and reionization bumps (the latter peaking at $\ell < 10$), with greater sky and frequency coverage (LiteBIRD Collaboration et al. 2023). Together, these efforts are expected to improve current constraints on r by more than an order of magnitude.

Achieving this level of precision, however, requires overcoming a range of observational challenges. From the sky, the two dominant sources of contamination to the primordial B -mode signal are lensing-induced B -modes and Galactic foregrounds. Gravitational lensing by large-scale structure deflects CMB photons, converting part of the primordial E -mode polarization into B -modes, particularly at smaller angular scales ($\ell \gtrsim 100$) (Zaldarriaga & Seljak 1998; Lewis & Challinor 2006). Galactic emission dominates over the primordial B -mode signal at all frequencies and angular scales: synchrotron radiation from relativistic electrons in magnetic fields is strongest at lower frequencies ($\lesssim 60$ GHz), while thermal emission from aligned interstellar grains

becomes dominant at higher frequencies ($\gtrsim 100$ GHz) (Planck Collaboration et al. 2020a).

If the Galactic foreground emission exhibited a uniform spectral energy distribution (SED) across the sky (i.e., perfect correlation between frequencies), the removal of these B -mode foregrounds would be straightforward. One could measure each component at its dominant frequency (low for synchrotron and high for dust) and then simply scale the map to other frequencies using a single scalar parameter. However, spatial variation in the frequency dependence of the foreground SEDs results in “frequency decorrelation,” meaning that maps at different frequencies cannot be related by a simple multiplicative factor (Planck Collaboration et al. 2016a, 2017). In addition, the Galactic magnetic field structure can produce line-of-sight (LOS) variation in SED parameters, creating a frequency-dependent polarization angle known as “LOS decorrelation” (Tassis & Pavlidou 2015; Vacher et al. 2023b). When spectral parameters governing SEDs vary across the sky, computing angular power spectra from maps involves averaging over regions with different SEDs. Due to the non-linearity of the SED variation, the averaging leads to a phenomenon known as “SED distortion” such that even if every SED on every line-of-sight could be described by a simple parametric model, the averaged SED may not be able to be fit by the same model (Chluba et al. 2017).

For current experiments, these effects are particularly important for thermal dust emission, which may exhibit complex spectral behavior due to physical variations in both the dust temperature (T_d) and spectral index (β_d) throughout the interstellar medium. These variations can occur both spatially on the sky and along the LOS, as different dust populations with varying properties contribute to the observed signal. Synchrotron emission can also exhibit frequency decorrelation, primarily driven by spatial variations in its spectral index, although its contribution is typically subdominant at the frequencies targeted by upcoming experiments focused on detecting primordial B -modes.

The level of frequency decorrelation in polarized dust and synchrotron emission at millimeter wavelengths remains uncertain. Planck data have constrained a 97.5% dust correlation limit between the 217 and 353 GHz channels at 99.1% across scales $50 < \ell < 160$ over 71% of the sky (Planck Collaboration et al. 2020a). These global constraints do not rule out more significant decorrelation in smaller, localized regions. More targeted studies have probed line-of-sight decorrelation, revealing small-scale spatial variations in the decorrelation degree of the dust (Pelgrims et al. 2021; Ritacco et al. 2023). Complementary results from BICEP/Keck

find no significant decorrelation in clean, high-latitude regions relevant for primordial B -mode searches (Ade et al. 2023), whereas the SPIDER balloon experiment reports evidence for spatial variation in dust spectral behavior in similar regions (Ade et al. 2025). Importantly, viable models of dust polarization allow for decorrelation levels that can vary by orders of magnitude between 150 GHz and higher frequencies (Planck Collaboration et al. 2020a; The Pan-Experiment Galactic Science Group et al. 2025).

If unmodeled, decorrelation from spatial and line-of-sight variations in foregrounds spectral properties can bias component separation and lead to incorrect inferences of primordial B -modes (Remazeilles et al. 2016; Planck Collaboration et al. 2017). This effect is expected to be increasingly important for high-sensitivity experiments including the SO. The SO, a ground-based experiment located in the Atacama Desert, will observe the microwave sky in six frequency bands spanning 27–280 GHz. Initial observations are underway. Its Small Aperture Telescopes (SATs) are designed to target large-scale polarization over ~ 10 –20% of the sky, aiming to constrain $\sigma(r)$ to an uncertainty of 0.002–0.003 (Ade et al. 2019). At this sensitivity level, characterizing and mitigating possible biases arising from mismodeling the effects of frequency decorrelation is important for robust component separation and cosmological inference.

A commonly used approach in current and past CMB analyses is the cross-spectrum (C_ℓ -based) component separation method, where auto- and cross-power spectra between frequency channels—particularly in B -modes—are used to construct a data vector that is fit with a model of cosmological and Galactic components (e.g., BICEP/Keck Collaboration et al. 2016, 2021; Planck Collaboration et al. 2016b, 2020b). This method is especially well suited to ground-based experiments, where complex time-stream filtering and spatially inhomogeneous, non-white noise introduce non-trivial correlations between pixels, making map-based likelihoods challenging to implement reliably (e.g., Hervías-Caimapo et al. 2025). In its simplest form, the C_ℓ -based approach assumes perfect frequency correlation of foregrounds, i.e., that the foreground signal at a given frequency can be extrapolated from a template at a pivot frequency with a single parametrized spectral scaling.

To relax this assumption, analytic extensions based on moment expansions have been developed to model frequency decorrelation more flexibly (Chluba et al. 2017; Azzoni et al. 2021; Remazeilles et al. 2021; Mangilli et al. 2021; Vacher et al. 2022; Azzoni et al. 2023; Carones & Remazeilles 2024). While these extensions have shown

success in mitigating possible biases in the inferred cosmological parameters, it remains relatively unexplored which physical aspects of foreground complexity — such as spatial variation in the spectral parameters, LOS mixing, correlations between spectral parameters and foreground amplitudes — are primarily responsible for producing these biases. Recent work by Vacher et al. (2024) investigated aspects of this question in the context of the *LiteBIRD* mission, using map-based component separation, with a spin-moment expansion to model LOS dust variations, and showed that unmodeled moment complexity can bias r , reinforcing the need for physically motivated foreground models. Given the current uncertainties in the level and origin of frequency decorrelation, and the growing use of increasingly complex yet observationally plausible foreground models, it is important to identify which aspects of this complexity impact cosmological inference the most, and to assess the robustness of existing mitigation strategies in such regimes.

In this work, we build on the spectrum-based B -mode analysis described in Wolz et al. (2024) (referred to there as “pipeline A”) for application to SO, working towards quantifying the impact of frequency decorrelation on the measurement of r using state-of-the-art foreground simulations. By using physically parametrized models, we separately study the impact of spatial variations in the dust temperature, T_d , and the dust spectral index, β_d , on estimates for r . We also approximately assess the likely impact of line-of-sight (LOS) frequency decorrelation of the foregrounds, which would result in a frequency-dependent polarization angle, on estimates of r . To achieve this goal, we simulate different foreground realizations to assess how foreground complexity affects the C_ℓ -based component separation method. In this paper, Section 2 describes the simulations for the analysis, Section 3 summarizes the cross C_ℓ foreground cleaning formalism, Section 4 analyzes the effects of foreground complexity on estimates of r , Section 5 presents a discussion of the results, and Section 6 concludes with a summary.

2. SIMULATIONS

This section describes the simulations we use for the study. We generate simulations using the HEALPix¹ pixelization scheme (Górski et al. 2005) at a resolution of $N_{\text{side}} = 512$. This resolution is consistently used for foreground amplitude and SED parameter templates. Each realization includes four data splits, each with independent noise, and each split contains six channels corre-

¹ <https://healpix.sourceforge.io>

Frequency (GHz)	27	39	93	145	225	280
FWHM (arcmin)	91	63	30	17	11	9
N_{white} ($\mu\text{K}\cdot\text{arcmin}$)	46	28	3.5	4.4	8.4	21
ℓ_{knee}	15	15	25	25	35	40
α_N	-2.4	-2.4	-2.5	-3.0	-3.0	-3.0

Table 1. Simulation specifications for the SO SAT frequency channels. Noise parameters correspond to homogeneous white noise levels (N_{white}) and $1/f$ noise characterized by a multipole knee (ℓ_{knee}) and spectral index (α_N). FWHM values denote the beam size at each frequency. Inhomogeneous noise is modeled by modulating the homogeneous noise with the SO SAT hit-count map, as commonly done in SO simulations (e.g. [Azzoni et al. 2021](#); [Wolz et al. 2024](#)).

sponding to the SO SAT frequency bands centered at 27, 39, 93, 145, 225 and 280 GHz.

The simulated maps include both sky signal and instrumental noise and are similar to those in [Wolz et al. \(2024\)](#), with differences noted where relevant. The sky signal comprises the CMB (with input $r = 0$) and Galactic foregrounds, specifically dust and synchrotron emission, with different degrees of complexity, as described below in Section 2.3. Each signal is convolved with a Gaussian beam with FWHM at each frequency listed in Table 1. To simplify the simulations relative to expected observations, we assume δ -function passbands for each channel.

2.1. Noise

Following [Ade et al. \(2019\)](#), we model the noise as a combination of white and red components, with the noise power spectrum given by

$$N_\ell = N_{\text{white}} \left(1 + \left(\frac{\ell}{\ell_{\text{knee}}} \right)^{\alpha_N} \right), \quad (1)$$

where N_{white} is the white noise level, ℓ_{knee} and α_N characterize the low-frequency ($1/f$) noise and filtering effects. We adopt the “baseline optimistic” noise scenario defined in [Ade et al. \(2019\)](#), with specifications for the parameters listed in Table 1. As in [Wolz et al. \(2024\)](#), homogeneous noise maps are generated from Gaussian realizations of the theoretical N_ℓ . To produce inhomogeneous noise, we modulate these maps using the SO SAT hit-count map provided in [Ade et al. \(2019\)](#).² This approach does not fully capture the complexity of the SO noise model, including its anisotropic properties and the impact of filtering on the data ([Hervías-Caimapo et al.](#)

² We note that the sky coverage now used in the SO observations has evolved from this forecast version, but we do not expect this difference to affect the conclusions of this work.

[2025](#)). However, it provides a reasonable approximation for studying the impact of foreground complexity. Each data split within a simulation uses independent noise realizations.

2.2. CMB

CMB maps are generated as Gaussian realizations of the best-fit ΛCDM cosmological model from [Planck Collaboration et al. \(2020b\)](#), drawn from a theory spectrum computed using the Python package CAMB ([Lewis & Bridle 2002](#)). The simulations include lensing-induced B -modes but no primordial B -modes (i.e., $r = 0$).

We generate 500 CMB realizations for estimating covariance matrices, described in the following section. For component separation tests, we produce 100 independent CMB realizations per foreground scenario (see Section 2.3).

2.3. Foregrounds

Polarized foreground contamination is dominated by Galactic dust and synchrotron emission. We simulate a suite of both Gaussian and more realistic foregrounds: the Gaussian simulations are used for covariance estimation and pipeline validation, while the non-Gaussian simulations are essential for evaluating the impact of spatial and spectral complexity on component separation performance and the robustness of constraints on r . We also consider simulations with mixtures of non-Gaussian and Gaussian components. Table 2 summarizes the simulation scenarios, and we refer to it throughout the following.

To summarize our simulation design, we categorize the scenarios into three classes:

The first class includes the *d10 Nominal*, β_d -*Spatial*, T_d -*Spatial*, and *LOS* scenarios. These form the core of our analysis and are used to examine how different aspects of dust complexity can bias the tensor-to-scalar ratio r , if the dust is incorrectly modeled. We use the *d10 Nominal* scenario to compare results to those obtained with the unmodified d10 dust foreground.

The second class consists of the *Simple Gauss*, β_d *Gauss*, and β -*Dust Corr.* scenarios. These Gaussian simulations serve both as benchmarks for comparison with previous studies and as the basis for covariance construction. Their controlled statistical properties—such as the level of non-Gaussianity and the correlation between β_d and dust amplitude—make them useful for isolating the effects of frequency decorrelation on χ^2 values and for exploring the influence of β_d -dust correlations on possible biases of r .

The last class comprises all *Ad10*Bd** and *Ad10Bd10 rot* scenarios. This class is designed to diagnose the ori-

gin of the biases in r that we find in this study. In particular, the $Ad10^*Bd^*$ scenarios construct dust signals with Gaussian and d10 dust amplitude and β_d . The $Ad10Bd10\ rot$ scenario is designed to investigate the mechanism that we find gives rise to biases in r .

2.3.1. Non-Gaussian Foregrounds

DUST

We construct a custom suite of realistic dust models based on the d10 model from the PySM3 package (Thorne et al. 2017; Zonca et al. 2021; The Pan-Experiment Galactic Science Group et al. 2025). The d10 model is built from the Planck Generalized Needlet Internal Linear Combination (GNILC) dust maps (Remazeilles et al. 2011; Planck Collaboration et al. 2020c). It uses the Planck PR3 GNILC Q/U polarization maps as large-scale spatial templates. SED parameters—dust spectral index β_d and temperature T_d —are based on fits to the Planck PR2 GNILC-derived maps (Planck Collaboration et al. 2016c). The d10 model combines these large-scale templates with small-scale fluctuations in both the structure of the polarized dust emission and the parameters of the dust SED. The resulting templates are scaled to each observation frequency using a single-component modified blackbody in each pixel, as described in The Pan-Experiment Galactic Science Group et al. (2025).

The distribution of β_d values within the sky area considered for SO analysis is shown in Figure 1. As shown in Figure 2, we find that a power law in ℓ provides an acceptable fit to the BB power spectrum of the dust map at 280 GHz, with $\chi^2 = 40$ for 27 dof (PtE of 0.05), where the map includes simulated SO noise described in Section 2.1. Figure 3 shows the 217×353 GHz BB cross-spectra for d10 dust and Planck PR4 measurements (Planck Collaboration et al. 2020d). The feature near $\ell \sim 100$ in the d10 power spectrum—where it deviates most prominently from a power law—is qualitatively consistent with Planck PR4 measurements, which also show significant departures from a pure power law in this multipole range.

In this study we quantify dust complexity using the frequency decorrelation between the 217 GHz and 353 GHz channels, defined as $1 - \mathcal{R}_\ell^{217 \times 353}$, where the spectral correlation ratio $\mathcal{R}_\ell^{217 \times 353}$ is

$$\mathcal{R}_\ell^{217 \times 353} = \frac{C_\ell^{217 \times 353}}{\sqrt{C_\ell^{217 \times 217} C_\ell^{353 \times 353}}}, \quad (2)$$

as defined in Planck Collaboration et al. (2017). We adopt this as our primary proxy for the complexity of a given foreground model, serving as a practical metric

to guide our dust model modifications. It is just one of several manifestations of foreground spectral complexity — others include polarization angle rotation, SED distortions, and the frequency dependence of the EE/BB ratio (Azzoni et al. 2021; Vacher et al. 2023a).

The Planck collaboration placed a 97.5% limit of $\mathcal{R}_\ell^{217 \times 353} \geq 0.991$ on the spectral correlation parameter for $50 < \ell < 160$ over the Planck LR71 mask, covering a high-Galactic-latitude region with 71% effective sky coverage (Planck Collaboration et al. 2020a). Uncertainties were quantified based on end-to-end simulations incorporating a model of Galactic magnetic field structure, and are at the 0.005 level. Among existing PySM models, the d12 model based on the “layer model” of Martínez-Solaesche et al. (2018) produces decorrelation at a level comparable to this upper limit when evaluated over the LR71 mask (The Pan-Experiment Galactic Science Group et al. 2025). We therefore use d12 as a practical proxy for “maximal decorrelation” in our analysis to set the upper bound on spatial variation in the dust SED parameters even though the sky region in this work differs from LR71.

The SO SAT sky region is smaller than LR71, but the mean decorrelation level of d12 over the SO SAT region is only $\sim 5\%$ larger, well within the uncertainty estimated on this quantity from the Planck data. The d10 model has more decorrelation in the SO SAT region compared to LR71, with $1 - \mathcal{R}_\ell^{217 \times 353} = 0.005$ for the SO SAT region we consider, compared to 0.003 for LR71 for the $x_{\beta_d} = 1$ case of the β -Spatial scenario. This difference is within the uncertainty on \mathcal{R} estimated from Planck. Given this sensitivity to sky region and the expectation that the decorrelation level will depend on the exact region chosen for the real SO analysis, we explore a range of decorrelation levels that reach at least the d12 level.

As a reference case, we create the *d10 Nominal* scenario, consisting of 100 noise realizations with unmodified d10 dust. These serve as a basis for comparing with different d10 variants in this study.

To isolate different physical effects, we separately model two sources of decorrelation: *spatial decorrelation*, arising from pixel-to-pixel variation in SED parameters, and *line-of-sight* (LOS) decorrelation, due to the superposition of multiple emission components with different spectra along the same line of sight. These are simulated using distinct approaches described below.

- **Spatial Decorrelation:** We model spatial decorrelation through spatial variation in the dust SED parameters β_d and T_d , corresponding to the β_d -Spatial and T_d -Spatial scenarios listed in Table 2. In this case, decorrelation arises from anisotropic

Scenario	Synch	β_s	Dust	β_d	T_d	Scaled	Scaling	N_{case}	N_{sims}	N_{cov}	Section
d10 Nominal	s5	s5	d10	d10	d10	β_d	1.0	1	100	-	2.3.1
β_d -Spatial	s5	s5	d10	d10	$\langle d10 \rangle$	β_d	$[0, 2.]; 0.2$	11	1100	-	2.3.1
T_d -Spatial	s5	s5	d10	$\langle d10 \rangle$	d10	T_d	$[0, 4.]; 0.4$	11	1100	-	2.3.1
LOS	s5	s5	d10	Q: d10 U: $\langle d10 \rangle$	$\langle d10 \rangle$	β_d^Q	$[0, 2.]; 0.2$	11	1100	-	2.3.1
Simple Gauss	PL	-3.	PL	1.54	19.6 K	-	-	1	600	1	2.3.2
β_d Gauss	PL	BPL	PL	BPL	19.6 K	β_d	$[0, 12.5]; 2.5$	6	600	6	2.3.2
β -Dust Corr.	PL	BPL	PL	BPL	19.6 K	β_d	12.5	1	100	-	2.3.2
Ad10Bd10	PL	BPL	d10	d10	19.6 K	β_d	1.6	1	100	-	2.3.3
Ad10Bdg	PL	BPL	d10	BPL	19.6 K	β_d	10.	1	100	-	2.3.3
Ad10gBd10	PL	BPL	d10g	d10	19.6 K	β_d	1.6	1	100	-	2.3.3
Ad10gBdg	PL	BPL	d10g	BPL	19.6 K	β_d	1.6	1	100	1	2.3.3
Ad10Bd10 rots	PL	BPL	d10	BPL	19.6 K	β_d	1.6	4.	400	-	2.3.3

Table 2. Summary of all simulation scenarios used in this study. The details of each case are described in Section 2.3. “Synch” and “Dust” indicate the synchrotron and dust templates, respectively. The template can be a non-Gaussian map (s5, d10), or a Gaussian random realization from a power-law (PL) spectrum or from a power spectrum template (d10g). β_s , β_d , and T_d are SED parameters, which can be either a constant (a real value or the mean of a template in the SO SAT mask region such as $\langle d10 \rangle$), a realistic template (s5, d10), or a Gaussian random realization from a broken-power-law (BPL) power spectrum. The “Scaled” column indicates the SED parameter scaled under the scenario. The “Scaling” column indicates the scaling applied to the SED parameters. This scaling is either a constant or a range-increment pair, defined as x in Equation 3. N_{case} and N_{sims} are the number of cases and number of total simulations in each scenario, respectively. If the simulation scenario is used for calculating covariance, N_{cov} is the number of covariances constructed from this scenario. A detailed description of covariance estimation is presented in Section 3.2. The “ β -Dust Corr” scenario has non-zero β_d -dust correlation ($\langle \beta_d \cdot d \rangle \neq 0$), and the “Ad10Bd10 rots” scenario applies four different rotations to β_d of d10. The last column provides the section in which corresponding scenarios are described.

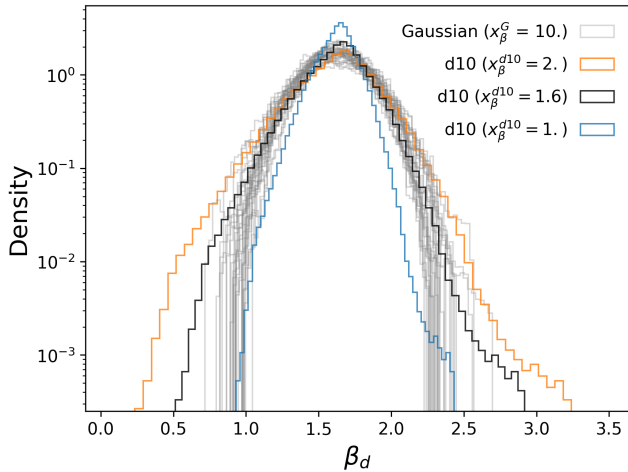


Figure 1. The distribution of dust emissivity indices, β_d , for the d10 simulation in the SO region without scaling (blue, $x_{\beta}^{d10} = 1.$), at the maximum scaling considered (orange, $x_{\beta}^{d10} = 2.$), and at the scaling that matches the degree of decorrelation in the d12 simulation (black, $x_{\beta}^{d10} = 1.6$). These are compared to 30 Gaussian realizations (gray), scaled to $x_{\beta_d}^G = 10$, with resulting frequency decorrelation that matches that of the $x_{\beta}^{d10} = 1.6$ case.

sion in either β_d or T_d leads to stronger frequency decorrelation.

To construct these models, we start from the d10 SED templates and scale the spatial fluctuations of a chosen SED parameter θ within the SO SAT patch by a scalar factor x , while preserving the mean (monopole) amplitude of the original template:

$$\theta(\hat{n}, x_\theta) = (\theta(\hat{n}) - \bar{\theta}) \cdot x_\theta + \bar{\theta}, \quad (3)$$

where $\theta(\hat{n})$ is the unscaled template and $\bar{\theta}$ its spatial mean within the SAT footprint. \hat{n} determines the template pixel location. The standard deviation of θ is then directly proportional to x with this scaling relation. In each simulation, only one parameter (β_d or T_d) is varied at a time, while the other is held fixed³. For T_d , we impose a physical lower bound of 2.725 K, to avoid unphysical temperatures.

An important caveat to this procedure arises because the d10 templates exhibit a strong anti-

maps of SED parameters, where increasing disper-

³ This procedure could, in principle, also be applied to synchrotron parameters such as β_s , though we focus here on dust-related variations.

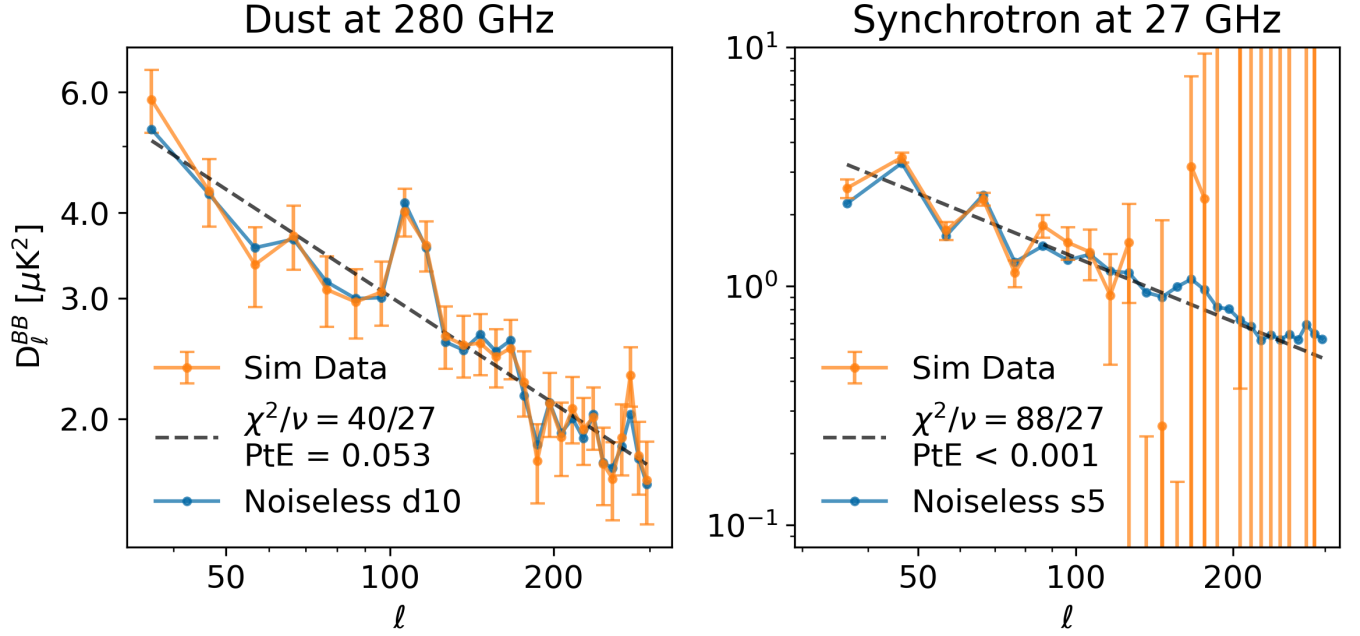


Figure 2. The angular power spectra of the d10 dust simulation at 280 GHz (left), and the s5 synchrotron simulation at 27 GHz (right), calculated in the SO-SAT region used in this study. In each panel, the orange points shows the binned power spectrum of the simulated foreground maps with noise, and the blue show spectra for noiseless maps. The spectra are computed as the mean of cross-split spectra, described in Section 3. The errors shown, and their associated covariance matrix, are estimated using the ‘Cov1’ method described in Section 3.2. The black dashed line shows the best-fitting power law to the noisy spectra, with the χ^2 , degrees of freedom (ν), and probability-to-exceed (PtE) for the fits indicated. The power law is an acceptable fit to the 280 GHz dust spectrum, but a poor fit to the 27 GHz simulated synchrotron spectrum at the larger scales.

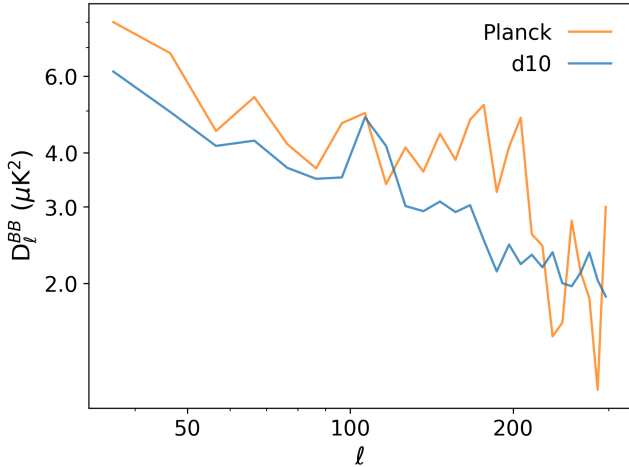


Figure 3. The 217 GHz \times 353 GHz BB cross-spectrum for the d10 dust simulation, compared to the Planck PR4 data, estimated over the SO-SAT region used in our analysis. At these frequencies the dust signal dominates the Planck spectrum. We note features departing from a pure power-law in both cases.

correlation between β_d and T_d . This anti-correlation could be the result of a fitting degeneracy known to impact data of low signal-to-noise ratio (Shetty et al. 2009). However, physical cor-

relations between β_d and T_d have been observed in laboratory measurements of interstellar dust analogues (Demyk et al. 2017). This anti-correlation has a counterintuitive effect: increasing the dispersion of one parameter (e.g., T_d) while holding the other fixed (e.g., β_d) at its original template can actually reduce the observed frequency decorrelation between 217 and 353 GHz. This occurs because the SED scaling anisotropies induced by the two parameters partially cancel out each other when anti-correlated, reducing the net SED scaling anisotropy across the sky and thus lowering the resulting frequency decorrelation.

Since this behavior obscures the intended relationship between SED parameter dispersion and its impact on r bias, we adopt a modified approach in the β_d -Spatial and T_d -Spatial scenarios (see 2): when varying one parameter, we fix the other globally to the average value of the original d10 template in the SO mask region, rather than using the full spatial map. This allows us to isolate the effect of β_d or T_d dispersion independently, avoiding the confounding influence of the strong anti-correlation present in the full d10 maps. Figure 1 shows the distribution of β_d

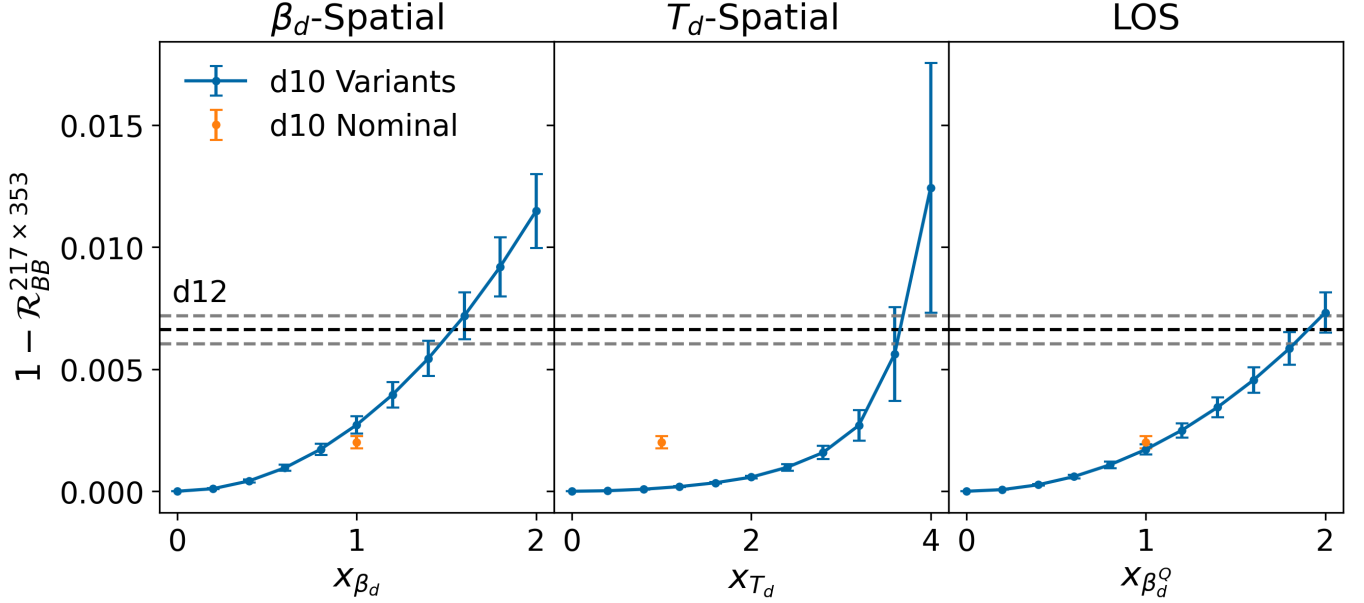


Figure 4. The degree of dust decorrelation ($1 - \mathcal{R}_{BB}^{217 \times 353}$) between the 217 GHz and 353 GHz simulated maps, calculated over the Planck LR71 mask and for scales $30 < \ell < 300$, as a function of dust parameter scaling, x . The three panels correspond to scaling the β_d field (left), the T_d field (middle) and the β_d field of just the Q Stokes maps to approximate line-of-sight decorrelation (right). The orange points in each panel show the decorrelation of the *d10 Nominal* dust simulation before our modifications. The x-axis scalings are specified in Section 2.3. The data points show the decorrelation values averaged over the bandpowers, using the same binning as in Figure 2, and the errors reflect the dispersion over the bandpowers. The gray dashed line indicates the mean and dispersion for *d12*.

within the SO mask region for several scenarios. We compare 30 Gaussian realizations scaled by $x_{\beta_d}^G = 10$ (gray, broken power law realizations defined in Section 2.3.2.) with the unscaled *d10* distribution (blue), the maximum *d10* scaling used in this study ($x_{\beta_d}^{d10} = 2$, orange), and an intermediate scaling ($x_{\beta_d}^{d10} = 1.6$, black), which approximately reproduces the decorrelation level of the *d12* model. The $x_{\beta_d}^G$ defines the scaling of the Gaussian dust β_d map, as described in Section 2.3.2. At larger values of x_{β_d} , the distribution of spectral indices extends beyond the range constrained by current observations in some regions.

The relationship between the scaling factor x in Equation (3) and the resulting frequency decorrelation is shown in Figure 4. We explore $x_{\beta_d} \in [0, 2]$ in steps of 0.2 and $x_{T_d} \in [0, 4]$ in steps of 0.4. At the highest values, the decorrelation reaches $1 - \mathcal{R}_{\ell}^{217 \times 353} = 0.012$, surpassing that of *d12*. These highly decorrelated cases allow us to probe pipeline performance beyond the complexity expected in current data. Notably, achieving a given level of decorrelation requires approximately twice as much scaling in T_d compared to β_d . This difference likely arises from the spectral behavior of thermal dust emission: with typical dust

temperatures around 20 K, the dust SED peaks well above the SO frequency range (approximately 500–700 GHz). In the Rayleigh-Jeans limit, the dust emission scales linearly with temperature perturbations in each pixel, so T_d variation changes the dust amplitude but not the shape of the SED at first order. As a result, SO observations are relatively insensitive to T_d variations, providing the motivation for neglecting T_d dispersion in Azzoni et al. (2021).

- **Line-of-sight Decorrelation:** This is the *LOS* scenario in Table 2. Line-of-sight decorrelation can arise when distinct dust populations along the line of sight have different SEDs and polarization angles, leading to the LOS-integrated Q and U Stokes parameters having different SEDs from each other. To simulate this effect in a simplified, artificial manner, we construct dust maps by combining the Q component from simulations with spatially varying β_d , and the U component from simulations with constant β_d ($x_{\beta} = 0$). This mismatch in spectral behavior between Q and U mimics the impact of LOS decorrelation. The resulting relation between the decorrelation level and the β_d^Q scaling factor is shown in Figure 4. The deliberate suppression of variation in β_d for the U component

naturally results in lower frequency decorrelation levels across the cases in the *LOS* scenario compared to those in the *Spatial- β_d* scenario.

Our implementation captures only one aspect of LOS decorrelation—namely, the spectral rotation of the polarization angle — while neglecting the breakdown of the modified blackbody assumption within individual pixels. Models like **d12** include more realistic LOS effects, but using them here would introduce confounding factors due to their inherent 2D spatial variations, making it difficult to disentangle the LOS contribution. Moreover, the **d10**-based model allows us to control the level of frequency-decorrelation in a manner consistent with other scenarios used in this study. A more systematic approach, such as constructing foreground models from moment maps or small scale filament structure (e.g., [Hervías-Caimapo & Hufnerberger 2022](#); [Vacher et al. 2024](#)), is left for future work.

SYNCHROTRON

To model realistic synchrotron emission, we use the **s5** model from the PySM3 Python package ([Thorne et al. 2017](#); [Zonca et al. 2021](#); [The Pan-Experiment Galactic Science Group et al. 2025](#)). This model provides a complex but observationally motivated description of polarized synchrotron at SO frequencies, helping maintain realism in our foreground simulations. At the angular scales relevant to this study, **s5** is formed using synchrotron emission using the Haslam 408 MHz intensity map and WMAP 9-year 23 GHz Q/U polarization maps as spatial templates. The frequency scaling is based on a spatially varying spectral index, β_s , from [Miville-Deschênes et al. \(2008\)](#) constructed using the Haslam 408 MHz map and the WMAP 3yr K band map ([Hinshaw et al. 2007](#); [Remazeilles et al. 2015](#)) and rescaled to match the level of β_s variation seen in a more recent analysis with S-PASS data ([Krachmalnicoff et al. 2018](#)).

Although the primary focus of this study is on the complexity of Galactic dust and its impact on measurements of r , we include the **s5** synchrotron model in our realistic foreground simulations to preserve fidelity to plausible sky conditions. We choose not to vary the synchrotron model across simulations to isolate the effect of dust complexity.

As shown in Figure 2, we find that a power law is a poor fit to the synchrotron power spectrum at 27 GHz,

especially at $\ell < 80$, with $\chi^2 = 88$ for 27 dof (PtE < 0.0005)⁴.

2.3.2. Gaussian Foregrounds

We generate Gaussian foreground realizations for both synchrotron and dust by sampling from the power-law angular power spectrum model

$$D_\ell = \frac{\ell(\ell+1)}{2\pi} C_\ell = A_c^{CC} \left(\frac{\ell}{\ell_0} \right)^{\alpha_c^{CC}}, \quad (4)$$

where $c \in \{d, s\}$ denotes dust and synchrotron respectively, $CC \in \{EE, BB\}$ denotes the polarization, A_c is the amplitude and α_c is the spectral index. We fix the pivot scale to $\ell_0 = 80$. These realizations are generated at the pivot frequencies and scaled to other frequencies using the SED models. In the Rayleigh-Jeans temperature units, the synchrotron SED follows a power law, and the dust SED follows the modified blackbody:

$$S_{\nu_0^d}^{d,\nu} = \left(\frac{\nu}{\nu_0^d} \right)^{\beta_d} \frac{B(T_d, \nu)}{B(T_d, \nu_0^d)}, \quad (5)$$

$$S_{\nu_0^s}^{s,\nu} = \left(\frac{\nu}{\nu_0^s} \right)^{\beta_s}, \quad (6)$$

where $B(T_d, \nu)$ is the blackbody function and we fix the dust temperature to $T_d = 19.6$ K. The resulting maps are then converted to CMB temperature units. The Gaussian foreground parameters are listed in Table 3.

We also generate a variant, referred to later with the label “Ad10g,” whose dust amplitude is drawn instead from a power spectrum estimated from the **d10** dust simulation at 353 GHz, whose shape is shown in Figure 2. We construct this by interpolating the binned noiseless dust *B*-mode power spectrum at 353 GHz in our sky region.

HOMOGENEOUS SED

This scenario corresponds to the *Simple Gaussian* row in Table 2, where spatially constant SED parameters are assumed across the sky. Specifically, the foreground maps at the pivot frequency are scaled to each SO channel using a single set of dust and synchrotron SED spectral parameters uniform across the sky. The case is equivalent to having $x_{\beta_d}^G = x_{T_d}^G = x_{\beta_s}^G = 0$ in Equation 3. We generate 500 Gaussian realizations for covariance matrix estimation and an additional 100 realizations for component separation testing in the simplest Gaussian case.

⁴ This statistic is computed using a Gaussian covariance estimated from idealized simulations, which may not fully capture the complexity of the foregrounds. This could lead to a mismatch between the assumed uncertainties and the true variation in the data, potentially inflating the χ^2 .

	$A_a^{EE} (\mu K_{\text{CMB}}^2)$	$A_a^{BB} (\mu K_{\text{CMB}}^2)$	α_a^{EE}	α_a^{BB}	β_a	T_a (K)
Dust	56.	28.	-0.32	-0.16	1.54	19.6
Synchrotron	9.	1.6	-0.7	-0.93	-3	-

Table 3. Summary of parameters used for Gaussian foregrounds. The angular power spectra parameters are defined in Equation (4). The SED parameters are defined in Equation (5) and Equation (6) for dust and synchrotron, respectively.

INHOMOGENEOUS SED

To compare with non-Gaussian foregrounds from the PySM model (Section 2.3.1), we also generate simulations with anisotropic SED parameters. Specifically, the β_d *Gauss* scenario in Table 2 corresponds to Gaussian simulations with inhomogeneous β that mimic the foreground SEDs of the “ β_d -Spatial” scenario described in Section 2.3.1. The β_d and β_s templates are drawn from a Gaussian field with a “broken power-law” angular power spectrum:

$$D_{\ell}^{\beta\beta,c} = \begin{cases} B_c \cdot \left(\frac{\ell}{80}\right)^{\gamma_c} & \ell \geq 15 \\ D_{\ell=15}^{\beta\beta,c} & \ell < 15 \end{cases} \quad (7)$$

where $c \in d, s$ refers to dust and synchrotron, respectively. The break at $\ell = 15$ suppresses large-scale power to reduce variance in the mean spectral indices over the SO mask region. The break also preserves the power-law form of the β templates within the analysis scale range $30 < \ell < 300$. We use the `synfast` routine in the `healpy` library to draw β_d and β_s templates as spin-0 fields, shifted by a mean value $\bar{\beta}_c$. The templates are based on power spectrum fits to the PySM d10 (for dust) and s5 (for synchrotron) models, with

$$\begin{aligned} B_d &= 3.682 \times 10^{-6} & \gamma_d &= -2.455 & \bar{\beta}_d &= 1.6 \\ B_s &= 0.611 \times 10^{-6} & \gamma_s &= -2.970 & \bar{\beta}_s &= -3.0. \end{aligned}$$

For dust, we fix the dust temperature to $T_d = 19.6$ K across the sky. The β_d template is then rescaled according to Equation 3 for $x_{\beta_d}^G \in [0, 12.5]$ in increments of 2.5.

The corresponding frequency decorrelation against β_d scalings are shown in Figure 5, where the highest-dispersion Gaussian case has similar decorrelation levels to the d10 model in the β_d -spatial configuration. The non-Gaussianity of the d10 β_d template leads to additional frequency decorrelation compared to a Gaussian realization of β_d with the same level of dispersion. The dust maps at the pivot frequency are scaled to the SO observation channels using the fixed dust temperature and the corresponding β_d maps. For each value of β dispersion, we generate 100 independent realizations.

Synchrotron β maps are held fixed across all dust β dispersion cases with $x_{\beta_s}^G = 1$. We generate 100 synchrotron realizations and reuse them for each of the Gaussian dust scenarios described above.

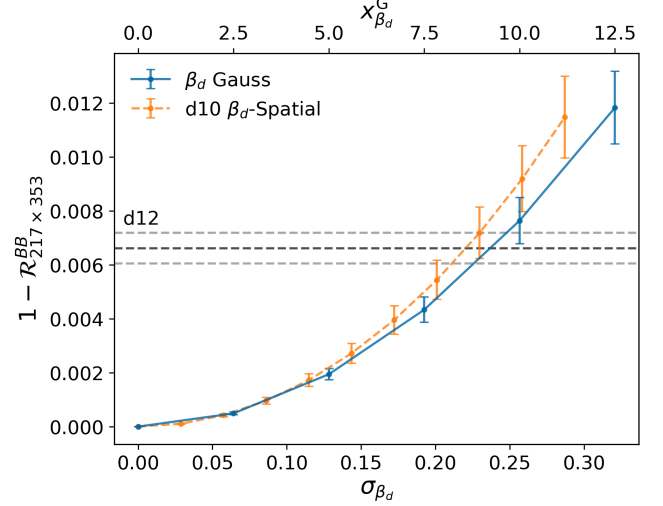


Figure 5. Frequency decorrelation over the Planck LR71 mask in the Gaussian simulations as a function of dispersion in β_d (σ_{β_d} , blue). The top x-axis label indicates the corresponding scaling factor, $x_{\beta_d}^G$. This is compared to the β_d -Spatial scenario (orange) from Figure 4. As in Figure 4, the d12 level is indicated.

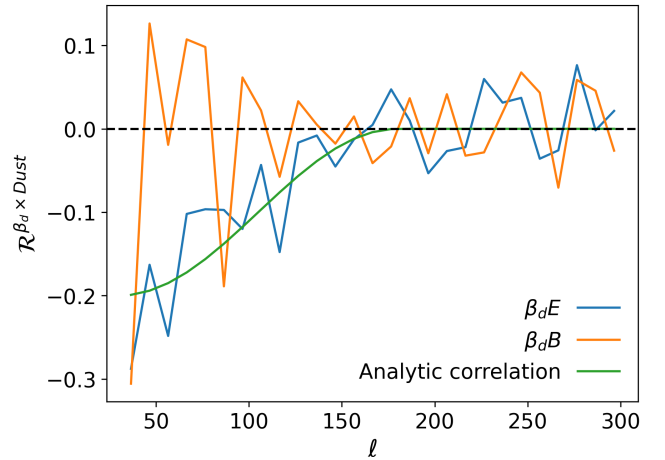


Figure 6. Comparison between the analytic correlation function ρ_{ℓ} (green, see Equation 8) and the empirical correlation, \mathcal{R}_{ℓ} , computed from the d10 β_d template map and the polarized d10 (Q, U) maps at 353 GHz, for E -mode (blue) and B -mode (orange) polarization. The analytic form is designed to approximate the scale-dependent behavior observed in the d10 model.

In addition to component separation tests, these Gaussian simulations are used to construct covariance matrices described in Section 3.2. These help quantify the impact of neglecting frequency decorrelation in the covariance matrices.

To investigate the potential impact of correlations between β_d and the dust amplitude map on estimates of the tensor-to-scalar ratio r , we also generate simulations that explicitly introduce such correlations. This corresponds to the β -Dust Corr. scenario in Table 2. Specifically, we jointly simulate the β_d and dust amplitude using the `synfast` routine from `healpy`, with the following set of input power spectra:

$$\begin{aligned} C_\ell^{TT} &= C_\ell^{\beta\beta,d} & C_\ell^{TE} &= \rho_\ell \sqrt{C_\ell^{\beta\beta,d} C_\ell^{EE,d}} \\ C_\ell^{EE} &= C_\ell^{EE,d} & C_\ell^{EB} &= 0 \\ C_\ell^{BB} &= C_\ell^{BB,d} & C_\ell^{TB} &= \rho_\ell \sqrt{C_\ell^{\beta\beta,d} C_\ell^{BB,d}}. \end{aligned}$$

This produces a spin-0 β_d map that is correlated with the Q and U dust amplitude maps. Here ρ_ℓ is a scale-dependent correlation function:

$$\rho_\ell = \begin{cases} -0.2 & \ell < 30 \\ -0.1 \cdot \left(\cos\left(\frac{\ell-30}{180-30}\pi\right) + 1 \right) & 30 \leq \ell \leq 180 \\ 0 & \ell > 180. \end{cases} \quad (8)$$

This functional form of the correlation is motivated by the observed relationship between the dust E -mode polarization and β_d in the **d10** model. We generate 100 realizations of simulations that incorporate this artificial correlation, where we fix the β_d dispersion at $x_{\beta_d}^G = 12.5$. If the correlation affects r bias, we expect its impact to be the strongest at maximum β_d decorrelation.

Figure 6 shows the analytic correlation function ρ_ℓ (green), alongside the empirical correlation \mathcal{R}_ℓ computed between the **d10** β_d template and the polarized **d10** (Q, U) maps at 353 GHz. The resulting \mathcal{R}_ℓ curves are shown separately for E -mode (blue) and B -mode (orange) polarization. Although the correlation between dust B -mode and β_d is consistent with zero, as shown in Figure 8, we construct this scenario with an imposed correlation to explicitly test the impact of a zeroth-order $\beta_d B$ correlation on the estimation of r .

2.3.3. d10-Gaussian mixture model

We generate an additional suite of simulations to investigate what properties of the dust can induce bias in the tensor-to-scalar ratio. We construct hybrid simulations combining Gaussian and non-Gaussian templates for the dust amplitude and β_d , in order to better identify which component's statistical non-Gaussianity is

primarily responsible for any bias in r . To isolate the dust contribution, we fix the synchrotron model to follow Gaussian simulations generated from power-law spectra and including spatially varying β_s , as described in Section 2.3.2. This setup captures realistic inhomogeneous SED effects.

We generate dust simulations where the β_d and amplitude maps are independently taken from either the **d10** template (Section 2.3.1) or the Gaussian dust simulations (Section 2.3.2). This allows for fully Gaussian, fully **d10**, or hybrid configurations combining elements from both.

To ensure consistent frequency decorrelation across cases, we fix the **d10** β_d dispersion scaling to $x_{\beta_d} = 1.6$ and scale the Gaussian β_d accordingly to match this **d10** frequency decorrelation between 353 GHz and 217 GHz. The dust temperature is fixed at $T_d = 19.6$ K for all simulations.

This simulation suite includes four combinations of dust amplitude and β_d maps, summarized as the *Ad10*Bd** scenarios in Table 2:

- *Ad10Bd10*: both amplitude and β_d maps from the **d10** template,
- *Ad10Bdg*: amplitude from **d10**, β_d from a Gaussian simulation,
- *Ad10gBd10*: amplitude from a Gaussian realization drawn from the **d10** template spectrum, β_d from **d10**,
- *Ad10gBdg*: amplitude from a Gaussian realization drawn from the **d10** template spectrum, β_d from a Gaussian simulation.

We generate 100 signal realizations for each configuration. For the configuration using the original **d10** amplitude and β_d maps (*Ad10Bd10*), only one dust realization is used. In this case, the CMB and synchrotron components vary across realizations, while the dust remains fixed.

We also construct a variant of the *Ad10Bd10* scenario, referred to as *Ad10Bd10 rots* in Table 2, in which four different coordinate rotations are applied to the β_d template prior to constructing frequency-dependent dust maps. These rotations intentionally misalign the β_d and dust amplitude templates, breaking their pixel-by-pixel correspondence when computing SED scalings. This simulation suite leverages the inhomogeneous structure of the β_d template and is designed to probe the impact of non-Gaussianity in β_d , and higher-order correlations between the dust amplitude and β_d templates, on any resulting bias in r . The β_d template for the nominal

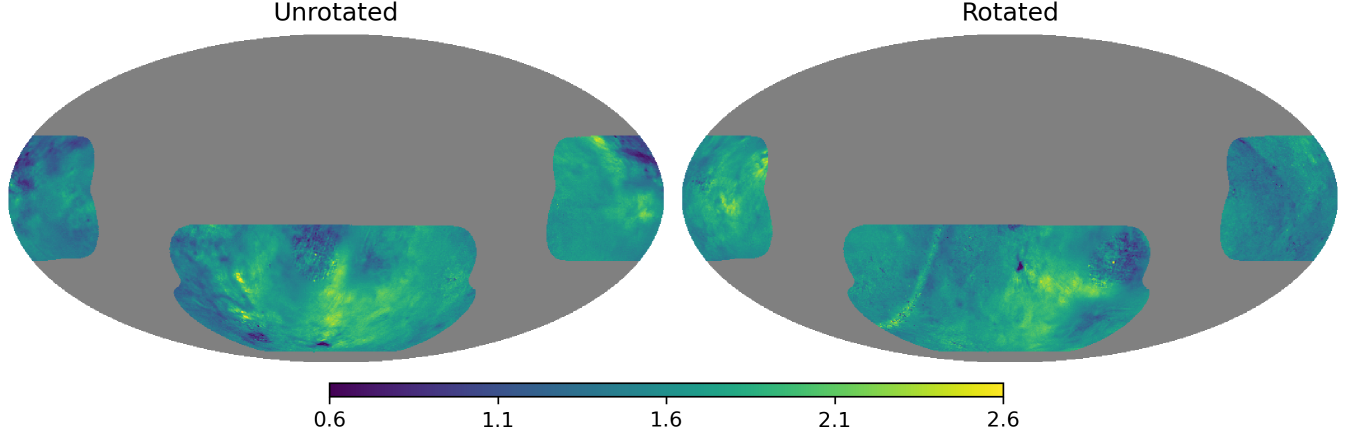


Figure 7. The β_d template for the nominal unrotated d10 simulation (left) compared with one of the rotated versions (right), within the SO mask. Both rotations exhibit pronounced non-Gaussian spatial structures, with the rotation shifting the location and orientation of these features across the sky.

unrotated d10 simulation is shown in Figure 7 together with one of the rotated versions.

3. PIPELINE

A widely used approach for foreground modeling in CMB B -mode analyses is the cross-spectrum (C_ℓ -based) likelihood formalism, which models CMB and foreground components parametrically in harmonic space. This method constructs a data vector from all auto- and cross-power spectra between frequency channels, $C_\ell^{\nu\nu'}$, and uses it in conjunction with an estimated covariance matrix to perform joint inference of cosmological and foreground parameters. The covariance captures contributions from sample variance, instrumental noise, and foreground uncertainties.

This approach is particularly well suited to ground-based experiments, where time-domain filtering and non-uniform, non-white noise introduce non-trivial pixel-pixel correlations that can be more easily treated in harmonic space. The cross- C_ℓ method has been successfully applied to real data analyses, including the tightest constraint on the tensor-to-scalar ratio, $r < 0.032 - 0.036$, from BICEP/Keck data combined with Planck and WMAP data (BICEP/Keck Collaboration et al. 2021; Tristram et al. 2022). It has also been benchmarked against alternative component separation approaches in the context of forecasting and simulation-based validation for SO (Wolz et al. 2024).

The version of the pipeline used in this work is implemented in the open-source BBPower software⁵, and is described in detail in Abitbol et al. (2021); Azzoni et al. (2021); Azzoni et al. (2023) and Wolz et al. (2024). This

pipeline consists of three major stages: power spectra computation, covariance matrix estimation, and parameter inference.

3.1. Power Spectra Computation

In this stage, we construct the data vector by computing auto- and cross-frequency B -mode power spectra of the six frequency channels from the simulated sky maps using the NaMaster package (Alonso et al. 2019). To mitigate E -to- B leakage caused by masking, we apply the B -mode purification feature in NaMaster (Lewis et al. 2001). We adopt the analysis mask used in Wolz et al. (2024), which is based on the hit-count forecast for SO from Ade et al. (2019) smoothed with a 10-degree “C1” apodization. Our analysis targets the multipole range $30 \leq \ell \leq 300$ of the SO SATs, which captures the recombination bump in the primordial B -mode signal, peaking at $\ell \simeq 80$. We assume that, in real data, the largest angular scales are significantly affected by atmospheric noise and filtering, while the smaller scales, primarily targeted by the SO-LAT and relevant for lensing B -modes, are not expected to carry significant primordial B -mode signal. We bin the power spectra uniformly with $\Delta\ell = 10$.

To mitigate instrumental noise bias, we split each simulation realization into multiple maps sharing the same sky signal (CMB and foregrounds) but with independent noise realizations (see Section 2.1). The polarized cross-power spectra are estimated by averaging over all unique cross-splits, excluding auto-split spectra to avoid noise bias. Specifically, for each pair of frequency channels (ν, ν') , we compute:

$$C_\ell^{\nu\nu'} \equiv \frac{1}{S(S-1)} \sum_{\{s, s' | s < s'\}} C_\ell^{\nu s, \nu' s'}, \quad (9)$$

⁵ <https://github.com/simonsobs/BBPower>

where $C_{\ell}^{\nu\nu'}$ is the cross spectrum between channel ν and ν' , S is the number of splits, and $C_{\ell}^{\nu s, \nu' s'}$ is the cross channel power spectrum calculated using channel ν from split s and channel ν' from split s' . In this work, we use four independent splits per simulation, resulting in six cross-spectra per channel pair. For $N = 6$ SO SAT frequency channels, the full data vector for one simulation contains $N(N + 1)/2 = 21$ spectra, or 567 data points, combining all cross- and auto-spectra.

3.2. Covariance Estimation

To estimate the bandpower covariance matrix, we consider three approaches, investigating the impact of including frequency decorrelation and deviations from a pure power-law shape in the foreground power spectra.

- In the first approach ('Cov1'), we use 500 power-law Gaussian simulations described in Section 2 and labeled 'Simple Gauss' in Table 2. Each block of the covariance matrix corresponds to a pair of cross-frequency spectra. Consistent with findings in Azzoni et al. (2021), the covariance is dominated by diagonal elements within each block. To suppress statistical noise due to the finite number of simulations, we retain only the main diagonal and six nearest off-diagonal elements within each block, setting all other entries to zero. This effectively preserves correlations between each bin and its three closest neighbors on each side. Given the width of our bandpower bins, this corresponds to retaining correlations within $\Delta\ell = 30$. Assuming that correlations beyond this range are negligible, the impact of this truncation is expected to be minimal.

This simple covariance matrix assumes no frequency decorrelation in each foreground component and power-law foreground power spectra. These assumptions holds reasonably well for simpler foreground simulations used in previous studies (e.g., Wolz et al. 2024), but break down under more complex foregrounds such as the d10 dust model. When frequency decorrelation and the dust spectrum shape are not accounted for in the covariance matrix, the resulting fit yields inaccurate χ^2 values.

- A set of 'Cov2' matrices include the effects of frequency decorrelation. Specifically, 'Cov2' matrices use β_d Gauss simulations whose synchrotron and dust β templates are Gaussian realizations drawn from broken power laws. Each 'Cov2' matrix is computed using 100 Gaussian realizations. They

include only the zeroth-order (main diagonal) elements within each frequency block, to reduce statistical noise that becomes significant given the smaller number of simulations. The variant of Gaussian realizations used for this covariance are labeled ' β_d Gauss' in Table 2, and these realizations have varying degrees of decorrelation.

- A final 'Cov3' matrix uses the Gaussian realizations labeled 'Ad10gBdg' and includes both decorrelation at a single scaling ($x = 1.6$) and the non-power-law spectrum template to better capture the signal. As with 'Cov 2,' it is computed using 100 Gaussian realizations and includes only the main diagonal elements within each frequency block.

3.3. Parameter Inference

We approximate the cross-spectrum likelihood as Gaussian and estimate the posterior distribution using Markov Chain Monte Carlo (MCMC) sampling. While the exact power spectrum likelihood is inherently non-Gaussian (e.g., Hamimeche & Lewis 2008), the Gaussian approximation is well justified—as expected from the central limit theorem—in the limit of large sky coverage and a high number of independent modes per bandpower bin, particularly over the analysis scale range $30 < \ell < 300$. Given the observing strategy and sky coverage of the SO SATs, and following previous analyses that adopt this assumption (Planck Collaboration et al. 2014, 2020b; Azzoni et al. 2021; Azzoni et al. 2023; Wolz et al. 2024), we consider the Gaussian likelihood approximation to be sufficient for this work.

Our parametric signal model includes contributions from the CMB and diffuse Galactic foregrounds, with $D_{\ell} = D_{\ell}^{\text{CMB}} + D_{\ell}^{\text{fg}}$. The B -mode power spectrum is modeled using two parameters: the tensor-to-scalar ratio r and a rescaling parameter for the lensing amplitude A_{lens} ,

$$D_{\ell}^{\text{CMB}} = A_{\text{lens}} D_{\ell}^{\text{lens}} + r D_{\ell}^r, \quad (10)$$

where D_{ℓ}^{lens} is the lensing-induced B -mode power spectrum, and D_{ℓ}^r is the primordial B -mode power spectrum with $r = 1$. Both templates are computed using the Python package CAMB (Lewis & Bridle 2002) with the best-fit Λ CDM cosmological parameters from Planck Collaboration et al. (2020b).

The foreground contribution to the power spectrum consists of synchrotron, dust, and their cross-correlation,

$$D_{\ell}^{\text{fg}, \nu_i \nu_j} = D_{\ell}^{s, \nu_i \nu_j} + D_{\ell}^{d, \nu_i \nu_j} + D_{\ell}^{ds, \nu_i \nu_j}. \quad (11)$$

Parameters	A_{lens}	r	A_d	A_s	α_d	α_s	ϵ_{ds}	β_d	β_s	B_d	B_s	γ_d	γ_s
Type	TH	TH	TH	TH	TH	TH	TH	G	G	TH	TH	TH	TH
Mid	-	-	-	-	-	-	-	1.6	-3.0	5	0	-3	-3
Width	-	-	-	-	-	-	-	0.1	0.3	10	5	0.5	0.5

Table 4. Priors adopted throughout our analysis for the free parameters. The type of prior is either tophat (TH) or Gaussian (G). “Mid” indicates the central point of each prior distribution. “Width” means the half-width for top-hat priors and standard deviation for Gaussian priors. The parameters are defined in Section 3.3. Empty Mid and Width entries indicate that the tophat prior is sufficiently broad to have no impact on the MCMC chains.

At a given frequency, D_ℓ^s and D_ℓ^d are modeled as power law angular power spectra defined in Equation (4). Here we recall from Figure 2 that this model is not a good fit to the power spectrum of the **s5** synchrotron map at 27 GHz at the largest angular scales.

To model the frequency dependence ($\nu_i \nu_j$), we adopt the following scaling:

$$D_\ell^{c, \nu_i \nu_j} = S_{\nu_0^c}^{c, \nu_i} S_{\nu_0^c}^{c, \nu_j} D_\ell^{c, \nu_0 \nu_0}. \quad (12)$$

Here $S_{\nu_0^c}^{c, \nu}$ is the SED of the component $c \in \{s, d\}$ defined in Equation (5) and (6), and the pivot frequencies for synchrotron and dust are $\nu_0^s = 23$ GHz and $\nu_0^d = 353$ GHz, respectively. The cross-correlation between dust and synchrotron is modeled as

$$D_\ell^{ds} = \epsilon_{ds} \sqrt{D_\ell^s D_\ell^d}, \quad (13)$$

with ϵ_{ds} a free parameter controlling the correlation amplitude (Choi & Page 2015).

The baseline model therefore includes nine free parameters:

$$\{A_{\text{lens}}, r, A_d, A_s, \alpha_d, \alpha_s, \epsilon_{ds}, \beta_s, \beta_d\},$$

resulting in 558 degrees of freedom when fitting the data ($N_{\text{data}} - N_{\text{params}} = 567 - 9$).

This baseline pipeline assumes no spatial variation in foreground spectral parameters. To relax this assumption, we adopt the minimal moment-expansion approach from Azzoni et al. (2021), which has been shown to yield the tightest unbiased constraints on r in the more complex foreground simulations explored by Wolz et al. (2024). This extension incorporates spatial variation of β_d and β_s as two power laws,

$$C_\ell^{\beta_c \beta_c} = B_c \left(\frac{\ell}{\ell_0} \right)^{\gamma_c}, \quad c \in \{d, s\} \quad (14)$$

which introduces four extra free parameters:

$$\{B_d, B_s, \gamma_d, \gamma_s\}.$$

Here the B ’s are the amplitudes of power laws at pivot scale $\ell_0 = 80$, and the γ ’s are the indices⁶. Since the

power law index γ_c is poorly constrained at small amplitude B_c , we apply an upper prior bound to prevent divergence in the MCMC sampling. This scenario has 554 degrees of freedom ($567 - 13$).

We use the *emcee* package (Foreman-Mackey et al. 2013) to perform MCMC sampling of the joint posterior distribution of the free parameters. The priors on all parameters are summarized in Table 4. The analysis in BICEP/Keck Collaboration et al. (2021) showed that a prior on β_d is no longer needed; we do include it here but find that the recovered posterior distributions for β_d are much narrower than the prior width, indicating that the choice of prior does not significantly impact our results.

To explore dust’s deviations from a simple power-law angular spectrum (Equation (4)), we also test a model with the template shape used in the Ad10g simulation described in 2.3, constructed from the binned noiseless dust B -mode power spectrum at 353 GHz. We introduce an overall amplitude scaling parameter for the template, but do not allow its slope to vary. By estimating the template shape directly from the noiseless d10 simulation at 353 GHz, we effectively reduce the number of degrees of freedom by at least 27 (the number of band-power bins), since the total 280 GHz spectrum is signal-dominated and thus well described as a scaled version of the 353 GHz dust spectrum. There are now 12 model parameters, so we approximate that there are 528 degrees of freedom when fitting the template model to the d10 simulated data ($567 - 27 - 12$). When this same template model is fit to the Ad10g simulated data, those data are drawn from the template spectrum and have scatter, so the degrees of freedom are not reduced in the same way; we approximate that there are 555 degrees of freedom in this case ($567 - 12$).

Of course, such noiseless templates cannot be constructed in practice; with real data we would expect to handle such deviations from power law behavior by constraining the dust amplitude in each bin separately. We also note that interpolation can suppress spectral features after rebinning, potentially introducing small biases.

⁶ See Equations (2.7), (2.16) and (2.17) in Azzoni et al. (2021) for explicit expressions of the moment expansion terms.

4. RESULTS

4.1. Gaussian Scenario Results

We begin by validating the cross-spectrum pipeline using the *Simple Gaussian* scenario with the corresponding Gaussian covariance matrix. As shown by the green point in Figure 8 (top), the fiducial pipeline with no moment expansion recovers an unbiased estimate of the tensor-to-scalar ratio r , consistent with earlier results from Azzoni et al. (2021); Azzoni et al. (2023); Wolz et al. (2024), when $x_{\beta_d}^G = x_{\beta_s}^G = 0$. The corresponding best-fit χ^2 per degrees of freedom ν (bottom panel of the same figure) is close to unity, with PtE of 0.33, indicating good agreement between the model and the data.

Figure 8 (top panel) illustrates that r is increasingly over-estimated with increasing β_d dispersion for the β_d *Gauss* scenario, where the β_s dispersion is kept fixed at $x_{\beta_s}^G = 1$ for a mild synchrotron frequency decorrelation. The solid lines indicate the estimated r from the fiducial (blue) and the moment (orange) pipelines. In the fiducial case, the bias on r increases with β_d dispersion, up to a level of $\delta r = 0.03$, while the $x_{\beta_d}^G = 0$ case remains unbiased, even despite the presence of spatially varying synchrotron β_s . The moment pipeline significantly reduces this bias across all dispersion levels, with results consistent with $r = 0$ within 1σ for all but the highest dispersion case. A small negative bias is observed for $x_{\beta_d}^G < 10$ at the $< 0.25\sigma$ level, in agreement with the trends reported by Azzoni et al. (2021), where it was attributed to prior and volume effects. As discussed there, this bias could be mitigated by adopting an appropriate prior (e.g., a Jeffreys prior) or by using a profile likelihood approach.

The red point in the top panel of Figure 8 corresponds to the β -*Dust Corr.* scenario, in which β_d is correlated with the dust amplitude (Section 2.3.2). Specifically, the correlation is imposed at the lowest (linear) order—we do not constrain higher-order correlation, such as those between β_d^2 and the dust amplitude, which could also influence the observed bias. The bias on r recovered with the fiducial cross- C_ℓ pipeline in this scenario is statistically consistent with the corresponding β_d *Gauss* case (blue), where no such correlation is present, even at high levels of frequency decorrelation. This result suggests that correlations between β_d and the dust amplitude have a negligible impact on the inference of r under current assumptions.

The bottom panel of Figure 8 shows the best-fit χ^2/ν for the same set of simulations, estimated with the fiducial (blue) and moment (orange) cross- C_ℓ pipeline. When using the simple Gaussian covariance (solid lines), the χ^2 is too high and increases with β_d dispersion, indicating both a poor model fit due to unmodeled frequency

decorrelation, and also an incorrect covariance matrix. Even the $x_{\beta_d}^G = 0$ case shows elevated χ^2 , driven by synchrotron decorrelation from spatially varying β_s .

We find that incorporating frequency decorrelation into the covariance matrix, by including spatial variations of β_d in the simulations used to compute the covariance, restores χ^2 to values consistent with the number of degrees of freedom (dotted lines), underscoring the importance of including SED parameter dispersion in covariance modeling⁷. The χ^2 values shown by the dotted curve are computed using the updated covariance matrix, while retaining the best-fit model obtained with the simple covariance. We demonstrate in Section 4.3 that the updated covariance does not alter the best-fit model. With the modified covariance, the moment pipeline maintains a stable χ^2 across all cases, while the fiducial pipeline continues to show increased χ^2 with growing β_d dispersion. This is expected, as the fiducial model assumes a spatially uniform SED and is unable to account for β_d variation.

4.2. Realistic scenario results

We test three decorrelation scenarios in which frequency decorrelation is induced by spatial variations in either β_d , T_d , or along the line of sight (LOS), as described in Section 2.3.1. The relationship between the scaling parameter x and the resulting decorrelation ($1 - \mathcal{R}_\ell^{217 \times 353}$) for each case was shown in Figure 4.

Figure 9 summarizes the r constraints obtained for each scenario using realistic foreground models — **d10** for dust and **s5** for synchrotron (Section 2.3.1) with the Cov1. In the limit of zero dust parameter dispersion (i.e., $x_{\beta_d} = x_{T_d} = 0$), the fiducial cross-spectrum pipeline yields a non-negligible bias on r across all scenarios. This bias originates from synchrotron decorrelation due to spatial variations in β_s present in the **s5** model. In contrast, the minimal moment-extension of **BBPower** recovers unbiased r , demonstrating that modeling SED variations with a second-order expansion in β_s is sufficient in this regime.

In the β_d -*spatial* and *LOS* scenarios, we find that the bias on r in the fiducial pipeline increases with β_d or β_d^Q dispersion, up to large values of order $r = 0.1$. The moment-expansion pipeline substantially reduces this bias, remaining consistent with $r = 0$ at low dispersion levels. At higher dispersions, a substantial bias

⁷ Although this method is not applicable to real data, the results highlight that modeling the impact of foreground frequency decorrelation in the covariance could become necessary if the level of decorrelation is significant. A detailed investigation of this effect is beyond the scope of this work and is left to future study.

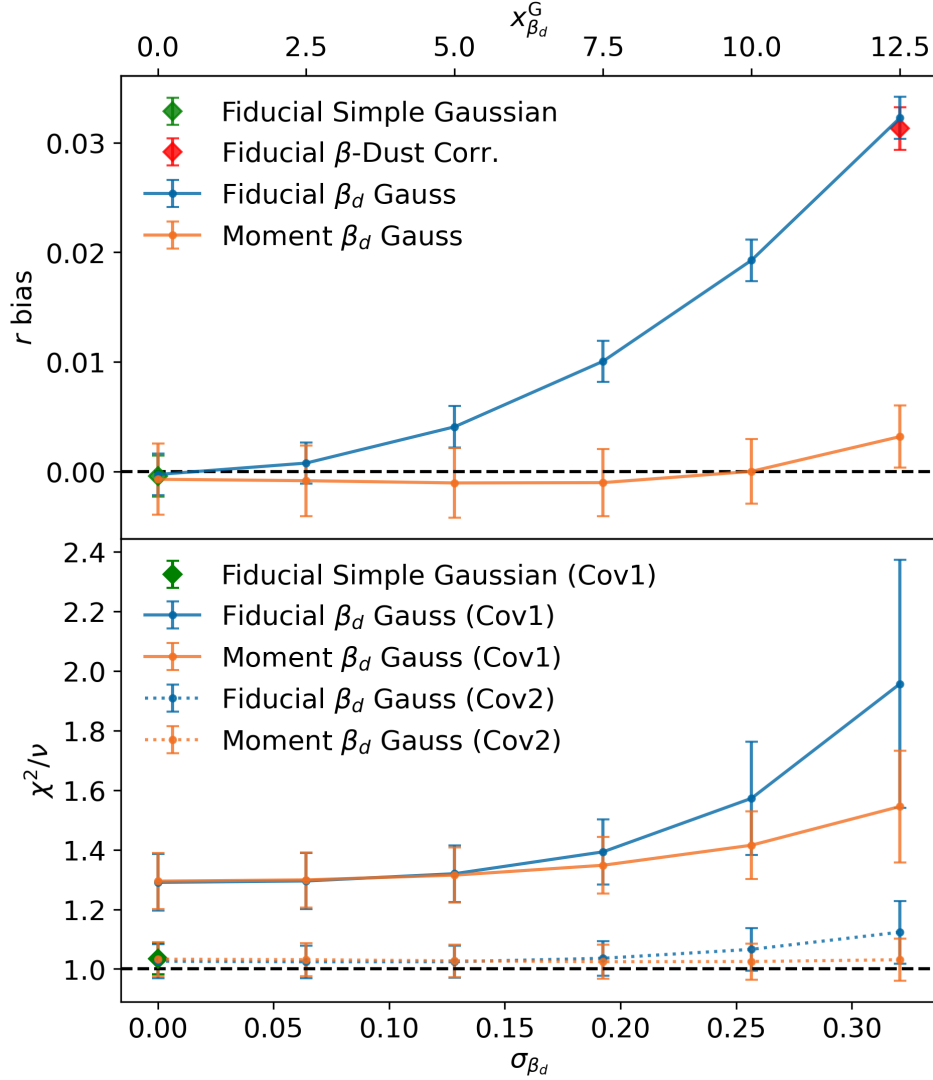


Figure 8. The bias in the recovered tensor-to-scalar ratio r (top) and corresponding χ^2 per degree of freedom (bottom) for Gaussian foreground simulations (β_d Gauss) with varying σ_{β_d} . The dashed black lines show the expected values for r (top, $r_{\text{input}} = 0$) and χ^2/ν (bottom). The solid lines show results from the fiducial (blue) and moment (orange) pipelines using the fully correlated Gaussian covariance (Cov1). Using the moment model removes the substantial bias in r , and the dotted lines show that the χ^2/ν is acceptable when using a covariance matrix that accounts for frequency decorrelation (Cov2). The green point shows the result for the *Simple Gaussian* case with no spatial variation in indices; in this case r is unbiased. The red point indicates the β -Dust Corr. scenario, where correlations between the β_d and the dust amplitude are included; this does not change the estimated r . Note that, even in the limit of $\sigma_{\beta_d} \rightarrow 0$, the simulation exhibit a non-zero level of frequency decorrelation due to the spatial variability of the synchrotron spectral index, leading to the constant offset from $\chi^2/\nu = 1$.

is still apparent, for $x_{\beta_d} \gtrsim 1.0$ in the β_d -spatial case and $x_{\beta_d^Q} \gtrsim 1.2$ in the LOS case.

The T_d -spatial scenario results in overall smaller biases in r for both pipelines. For $x_{T_d} \lesssim 2.0$, the r bias remains stable. At higher values, it begins to increase but remains below the bias observed at $x_{\beta_d} = 2.0$ in the β_d -spatial case, despite both configurations inducing similar levels of frequency decorrelation (Figure 4). This comparison should be interpreted with caution due to the larger uncertainty in frequency decorrelation at

$x_{T_d} = 4.0$ as shown in Figure 4. A more reliable comparison can be made between $x_{T_d} = 3.2$ and $x_{\beta_d} = 1.0$, where the decorrelation levels are comparable and uncertainties are better constrained. In this regime, both pipelines yield consistent biases on r across the scenarios, suggesting that the pipelines respond similarly to complexity induced by either β_d or T_d variations.

The parameter inference for these three scenarios uses the Cov1 covariance matrix, derived from Gaussian sim-

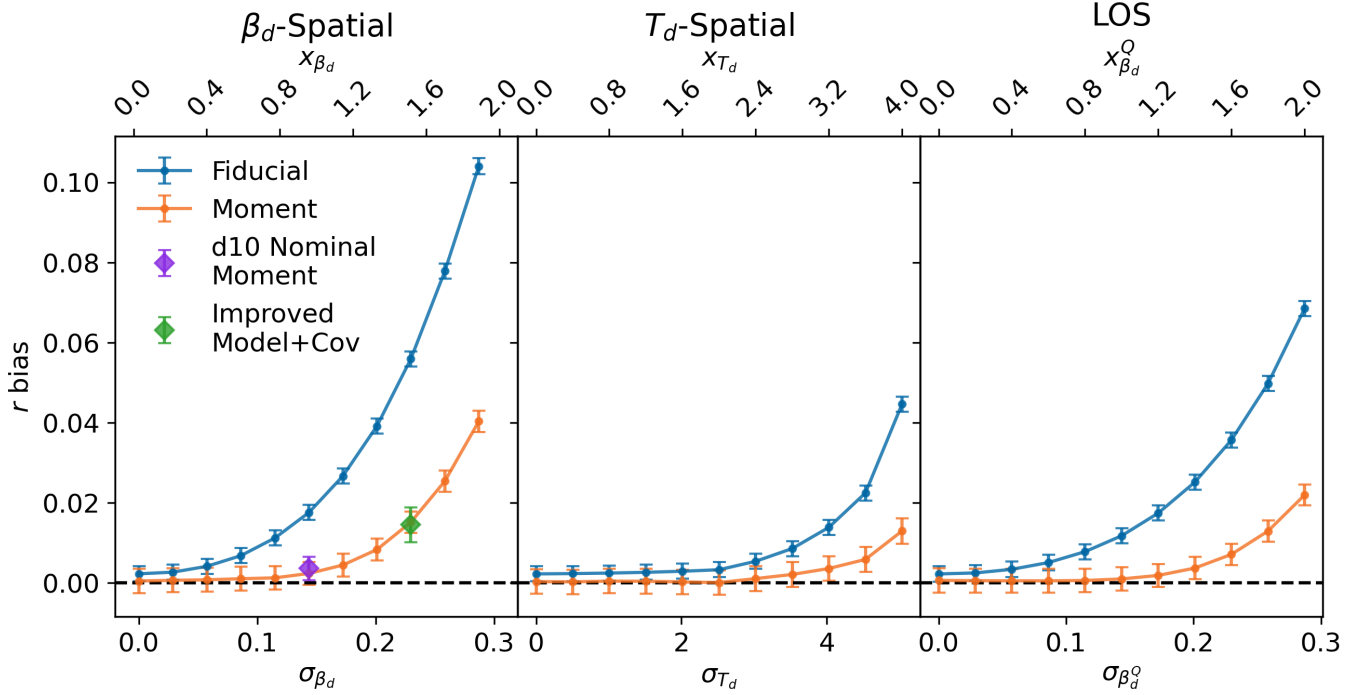


Figure 9. Recovered bias in r as a function of SED parameter dispersion (x-axis) for the non-Gaussian simulations with three realistic decorrelation scenarios: β_d -spatial (left), T_d -spatial (center), and LOS (right). Results are shown for the fiducial (blue) and moment method (orange), using the **d10** dust and **s5** synchrotron models. The fiducial pipeline shows an increasing bias in r as a function of dispersion, while the moment method mitigates bias at low to moderate levels—but unlike the Gaussian case shown in Figure 8, it does not remove it at the highest dispersion levels. The left-hand β_d -spatial case yields the largest bias for a given degree of decorrelation. For reference, the violet point in the left panel notes the result for the **d10 Nominal** scenario using the moment pipeline. The estimated value for r is consistent with the x_{β_d} case of the β_d Spatial scenario when we improve the modeling (angular spectral template) and the covariance (Cov3, including frequency decorrelation and angular spectral template), as shown by the “Improved Model+Covariance” case (green, left panel) for the $x_{\beta_d} = 1.6$ case, referred to in the text as *Ad10Bd10*.

ulations with power-law spectra and no frequency decorrelation, which is known to be incorrect. As in the β_d Gauss scenario, this approach leads to a significant overestimation of the χ^2 . For zero dust decorrelation ($x_d = 0$), the χ^2 per degree of freedom is 1.7, higher than the equivalent ~ 1.3 in the β_d Gauss scenario. We find that this increase is primarily driven by the synchrotron component in the simulated data, which is based on the **s5** template. Unlike the Gaussian synchrotron model used in the β_d Gauss test, **s5** introduces stronger frequency decorrelation and its SED deviates from a pure power-law, worsening the mismatch with the model assumed to compute the simple covariance and thereby increasing the χ^2 .

In this case, we find that incorporating synchrotron frequency decorrelation into the covariance⁸ does not

eliminate the χ^2 excess when $x_{\beta_d}^{d10} = 0$, only reducing the χ^2 per degree of freedom from 1.7 to 1.6. This behavior differs from that seen for the β_d Gauss scenario in Section 4.1, suggesting that additional effects are contributing to the elevated χ^2 . As discussed in Section 2.3.1, and shown in Figure 2, the angular power spectra of realistic dust and synchrotron (**d10** and **s5** here) depart from the pure power laws assumed in the Gaussian covariance.

To assess the impact of incorrectly assuming a power-law model in the simulations used to compute the covariance, we test the Cov3 matrix that captures the shape of the angular power spectrum at the dust-dominant frequency, and accounts for the cross-frequency correlations. We do this for a specific case: the *Ad10Bd10* simulation that combines power-law Gaussian synchrotron with **d10** dust, with $x_{\beta_d}^{d10} = 1.6$ (see Section 2.3.3). Using the nominal power-law model and the moment-expansion, we find a significantly improved fit, with χ^2

⁸ ‘Cov2’ that uses broken power law (BPL) β_s template scaled by $x_{\beta_s}^G = 6.4$ to match **s5** β_s spatial dispersion, with a constant β_d .

of 599 ± 33 for 554 degrees of freedom, with a PtE of 0.17⁹.

We also test a case where we use the power spectrum template shape in the model as well as in the covariance matrix. Here we find χ^2 of 564 ± 33 for 528 degrees of freedom and a PtE of 0.21 with the moment-expansion model. It appears that a power-law model for the dust, combined with a covariance matrix that accurately models the signal, is sufficient for the **d10** model at the adopted SO sensitivity. Higher sensitivity measurements may require more detailed modeling. Nonetheless, in some of our further investigations we choose to adopt the dust template shape in the model.

We find that these adjustments in modeling method and covariance matrix have a limited effect on the recovered value for r , as indicated by the green point in the first panel of Figure 9. The estimated r using the modified Cov3 covariance and modeling method differs by less than 0.2σ compared to using Cov1 and power law dust modeling. However, we find that the uncertainty using Cov3 is larger than that for Cov1, due to the inclusion of the decorrelations. This effect is expected to be a function of decorrelation level, and will be explored in future work. We do not reproduce all of the results in Figure 9 for the improved Cov3 covariance matrix.

4.3. Diagnosing the Origin of Biases in r

4.3.1. Role of β_d Complexity

We use a suite of mixture simulations that combine Gaussian and realistic models of dust and β_d (introduced as *Ad10*Bd** scenarios in Section 2.3.3) to investigate the source of the cosmological bias found, particularly when using the moment expansion method to model the simulated data. This approach, detailed in Azzoni et al. (2021), relies on several simplifying assumptions to characterize the multi-frequency power spectrum given spatial variations of foreground spectral parameters. Specifically, it assumes:

1. no line-of-sight (LOS) decorrelation,
2. spectral indices for each foreground component follow Gaussian distributions and are uncorrelated between different components,
3. amplitudes and spectral indices of each foreground component are uncorrelated,
4. amplitudes and spectral indices of each component are parametrized as power laws,

5. the expansion is truncated at leading order,

Based on the findings presented in the previous sections, certain assumptions, such as the correlation between amplitudes and spectral indices at lowest order (see Section 2.3.2 for discussion of the relevant simulations, and the red point in Figure 8) appear to be less critical sources of bias. Consequently, our analysis will primarily focus on assessing the impact of assumptions related to Gaussianity and the parametric form of the spectral models.

For testing, we adopt the Cov3 covariance matrix from the *Ad10gBdg* simulation, which includes both frequency decorrelation and the correct angular power spectrum shape. The component separation step uses the dust power spectrum template as the dust power spectrum model.

Figure 10 summarizes the r bias (δr), χ^2 , and PtE values for each combination of dust amplitude and β_d template. The top panel shows 2σ bounds of r compared to the input $r = 0$ (vertical dashed black line). Using the *Ad10Bdg* and *Ad10gBdg* scenarios, we recover similar r values of 0.0019 ± 0.0045 and 0.0023 ± 0.0045 , respectively, which are statistically consistent with zero. This indicates that the bias on r is not driven by non-Gaussianities in the realistic **d10** dust amplitude, consistent with the findings of Abril-Cabezas et al. (2024).

The *Ad10gBdg* scenario yields a χ^2 of 556 ± 34 for 555 degrees of freedom, with a PtE of 0.50, as expected for a well-specified model. In comparison, the *Ad10Bd10* scenario produces a slightly elevated χ^2 of 564 ± 33 for 528 degrees of freedom. Both cases demonstrate that incorporating a spectral template into the modeling, alongside a simulation-based covariance that reflects the same foreground complexity, is effective in mitigating χ^2 misestimation. Moving forward, while Gaussian realizations remain useful for covariance construction, future analyses should also consider analytical or semi-analytical covariance formulations to further suppress biases arising from mismatches in foreground modeling (e.g., Knox 1995; Atkins et al. 2024; Abril-Cabezas et al. 2024).

In contrast to the two Gaussian β_d scenarios, we find that using the **d10** β_d template introduces a bias in r regardless of the dust amplitude model. Both the *Ad10gBd10* scenario, which uses a Gaussian dust amplitude computed from the **d10** power spectral template, and the *Ad10Bd10* scenario, which uses the non-Gaussian Planck GNILC amplitude template, yield significant biases on r of 0.008 and 0.014, respectively. This indicates that the primary source of the bias is the **d10** β_d template itself. As shown in Section 4.1, this effect cannot be attributed to lowest-order correlations between dust intensity and β_d , suggesting that

⁹ Some residual χ^2 mismatch may also arise from interpolation artifacts introduced by the binned template.

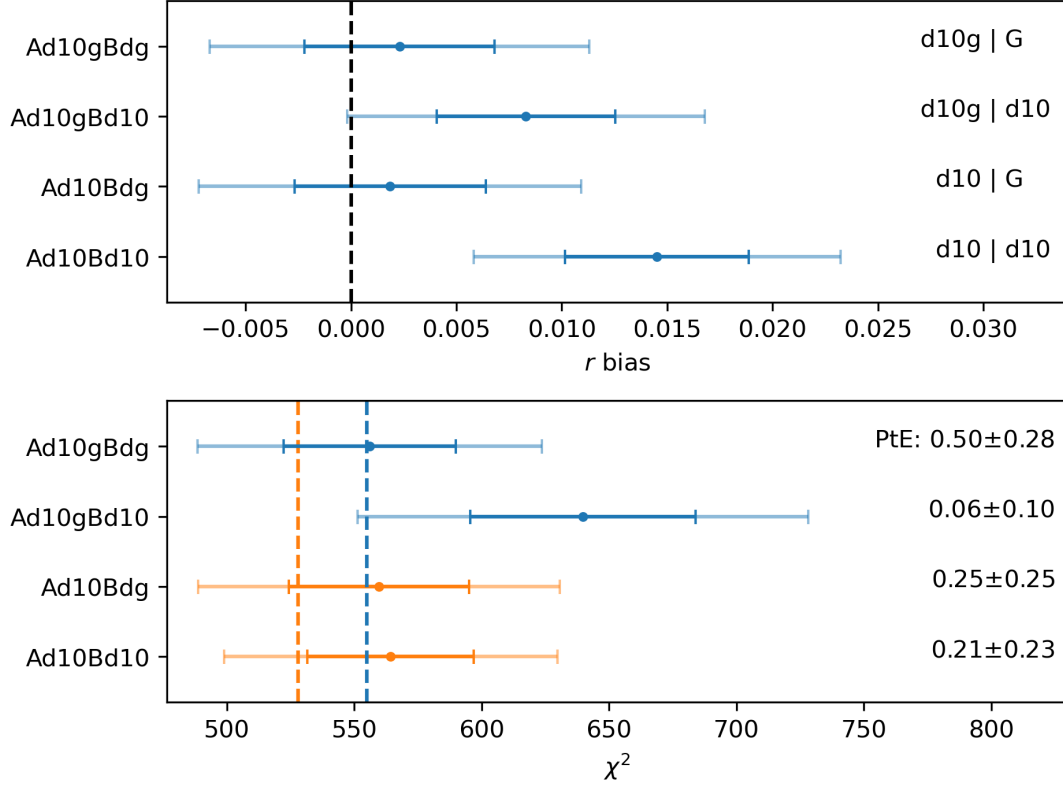


Figure 10. Top: 1σ and 2σ bounds for the estimated r for four **d10** mixture model scenarios that combine Gaussian and non-Gaussian maps for the dust amplitude and emissivity. The dust amplitude and β_d templates are labeled next to each scenario (amplitude | β_d), with the ‘g’ indicating a Gaussian map. Biases in r are only seen when the β maps are non-Gaussian. Bottom: 2σ bounds for the χ^2 values for the same scenarios. The degrees of freedom for **d10** (528, orange) and **d10g** (555, blue) amplitude templates are distinguished by the coloring. The PtE values for each scenario are labeled on the right.

higher-order statistical correlations between dust amplitude and β_d as well as non-Gaussian properties in the **d10** β_d field may be responsible.

Both **d10** β_d scenarios also exhibit worse χ^2 values, likely driven by poorer agreement with the cross-frequency spectra. The GNILC-derived β_d template appears less well-behaved, due to its inherent non-Gaussianity and higher-order correlation with dust amplitude, compared to Gaussian realizations drawn from a broken power-law model. These differences manifest in the cross-channel power spectra, degrading the quality of the fit and contributing to the increased biases in r .

4.3.2. Bias mechanism

In Section 4.1, we showed that the first-order correlations between β_d and dust amplitude do not contribute significantly to the bias in r . However, higher-order correlations, arising from either fitting degeneracies or physical processes, may still contribute.

To investigate this, we introduce the *Ad10Bd10* *rots* scenario described in Section 2.3.3, where we apply a set of four arbitrary coordinate rotations to the β_d map

within the SO patch. These rotations effectively preserve the statistical properties (e.g., dispersion, angular power spectrum) of the β_d field, while modifying any potential spatial or higher-order relationships with the dust amplitude map. We then propagate the rotated β_d templates through the component separation pipeline and estimate r . These are shown in Figure 11.

Despite the fact that the rotated β_d maps have nearly identical distributions and power spectra, both within each map and across different rotations as shown in Figure 12, we observe substantial variation in the r distributions. This indicates that neither the overall β_d dispersion nor its spectral shape is responsible for the bias. Moreover, the bottom panel of Figure 12 shows little correlation between frequency decorrelation and r bias, further suggesting that the overall dispersion plays a limited role in driving the bias on r in this scenario. Higher-order moments of the β_d distributions, such as skewness and kurtosis, also exhibit no clear correlation with the estimated r biases. Instead, it appears to originate from the specific spatial structure of β_d in each

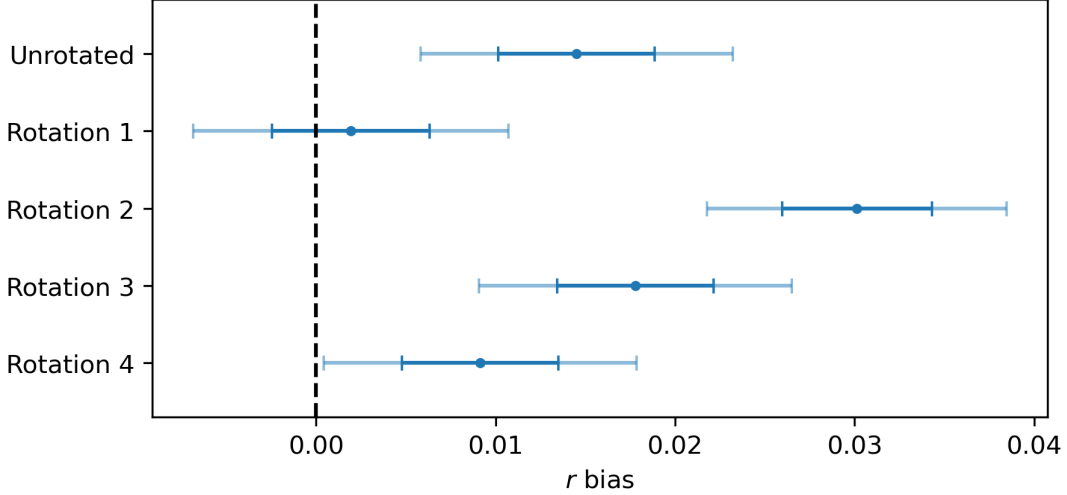


Figure 11. 1σ and 2σ bounds on the estimated r found using the moments method for the different *Ad10Bd10* *rots* cases. Four different coordinate rotations of the β_d map are compared to the standard unrotated **d10** case; the choice of rotation of the non-Gaussian β_d field has a large impact on the estimated r .

map, structure that is strongly spatially inhomogeneous, due to the physical distribution of dust on the sky.

Upon further investigation we find that certain configurations of the **d10** β_d map, under specific rotations, modify the low-frequency dust angular power spectra in a way that resembles a B -mode signal. Figure 13 shows the ratio of the 90 GHz and 280 GHz dust spectra under different β_d rotations. While the 280 GHz spectra remain largely unaffected (given their proximity to the 353 GHz pivot frequency), the 90 GHz spectra exhibit distinct ℓ -dependent SED scaling under different β_d rotations. Similar ℓ -dependence is also observed in prior studies (e.g., Chluba et al. 2017). The differences in power spectral ratios are therefore dominated by the ℓ -dependence of the 90 GHz dust power spectrum. In particular, some rotations, such as the standard **d10** and the Rotation 2, enhance large-scale ($\ell \lesssim 100$) power relative to small scales, producing a shape similar to the expected B -mode spectrum and resulting in a significant positive r bias. Other rotations, such as Rotation 1, maintain flatter scaling and avoid introducing significant bias.

4.3.3. ℓ -dependent SED effects

To understand the ℓ -dependent SED scaling of the dust power spectrum, we examine the power spectra of the moment-expansion dust maps. The β_d template can be expressed as a perturbation from the mean $\bar{\beta}_d$:

$$\beta(\hat{n}) = \bar{\beta} + \delta\beta(\hat{n}) \quad (15)$$

where \hat{n} denotes the position in the sky. The corresponding dust emission at frequency ν is given by the

moment expansion:

$$\begin{aligned} m(\nu, \hat{n}) &= \left(\frac{\nu}{\nu_0}\right)^{\bar{\beta} + \delta\beta(\hat{n})} \frac{B(T, \nu)}{B(T, \nu_0)} m(\nu_0, \hat{n}) \\ &= \left[\left(\frac{\nu}{\nu_0}\right)^{\bar{\beta}} \frac{B(T, \nu)}{B(T, \nu_0)} m(\nu_0, \hat{n}) \right] \\ &\quad \left[1 + \ln\left(\frac{\nu}{\nu_0}\right) \delta\beta(\hat{n}) + \frac{1}{2} \ln^2\left(\frac{\nu}{\nu_0}\right) \delta\beta(\hat{n})^2 + \mathcal{O}(\delta\beta^3) \right] \end{aligned} \quad (16)$$

where $m(\nu_0, \hat{n})$ denotes the dust amplitude template at pivot frequency, and $B(T, \nu)$ is the Planck law at $T = 19.6$ K. This moment expansion to the second order can be written as sum of three maps, or moment maps, that we call $m_0(\nu, \hat{n})$, $m_1(\nu, \hat{n})$, $m_2(\nu, \hat{n})$. These moment maps are powerful tools for interpreting foreground models (e.g., Vacher et al. 2024).

Figure 14 illustrates the power spectra of these moment maps in the β_d *Spatial* scenario for $x_\beta = 1.6$, where the β_d field remains unrotated. Since each n th-order moment map scales as $\ln^n\left(\frac{\nu}{\nu_0}\right)$, their contributions grow as the frequency moves away from ν_0 . This is especially significant at low frequencies, where higher-order terms begin to modify the dust power spectrum shape, leading to ℓ -dependent SED effects.

The top-right panel of Figure 14 compares the power spectra for selected combinations of moment maps. The 00, 00+11, and 00+11+22 curves correspond to zeroth-, second-, and fourth-order expansions (ignoring cross-moment correlations). While m_0 and m_1 contribute significantly, m_2 has negligible power.

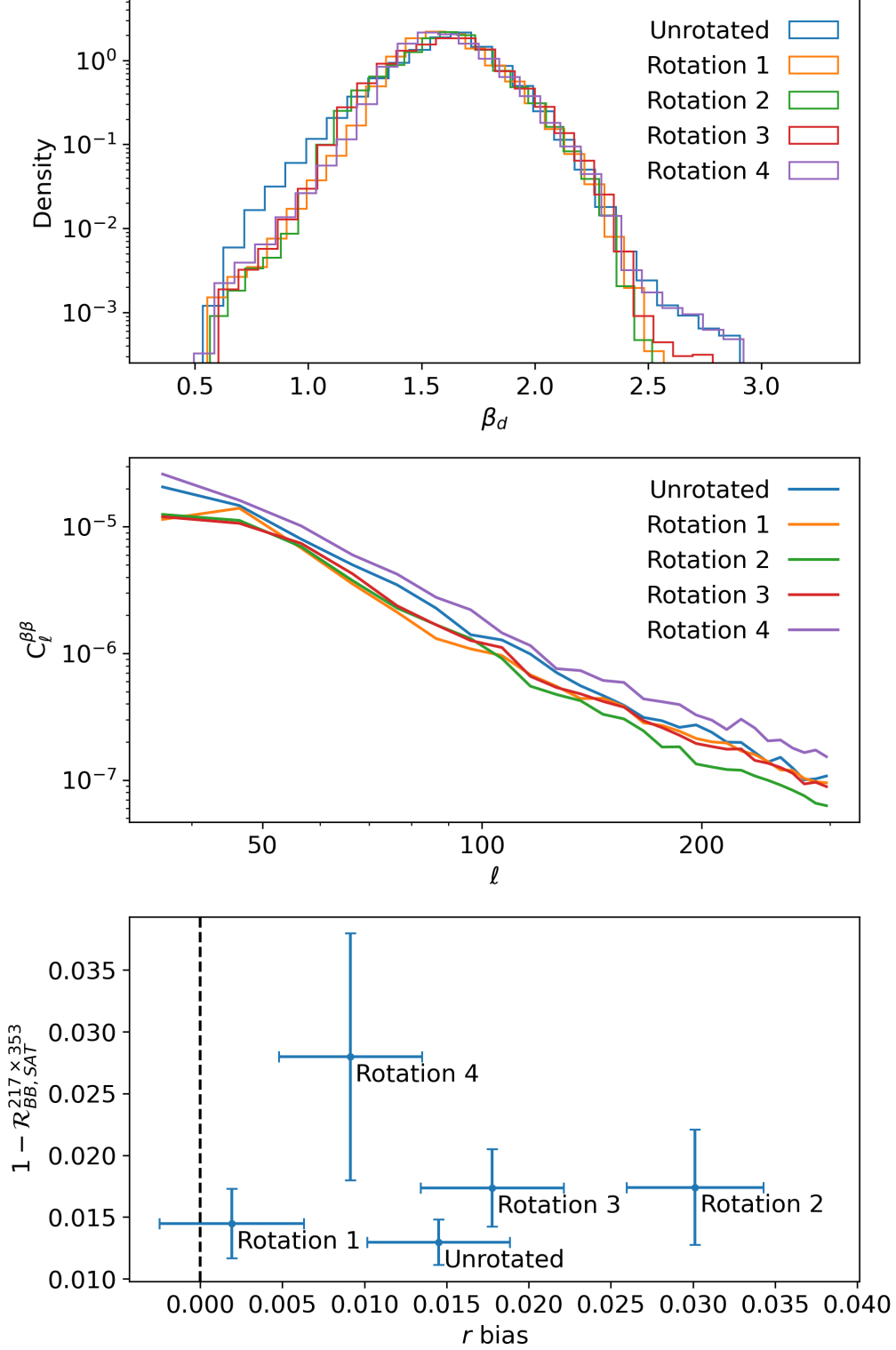


Figure 12. Selected properties of β_d under the four different rotations considered. The distributions for β_d (top), and the corresponding power spectra (middle), in our considered SO region. Both show small differences under different rotations, but without an obvious connection to the bias levels shown in Figure 11. Bottom: the decorrelation between the 217 and 353 GHz frequencies in the SO SAT mask, and the corresponding bias in r , for each rotation. There is not an obvious correlation between these two properties.

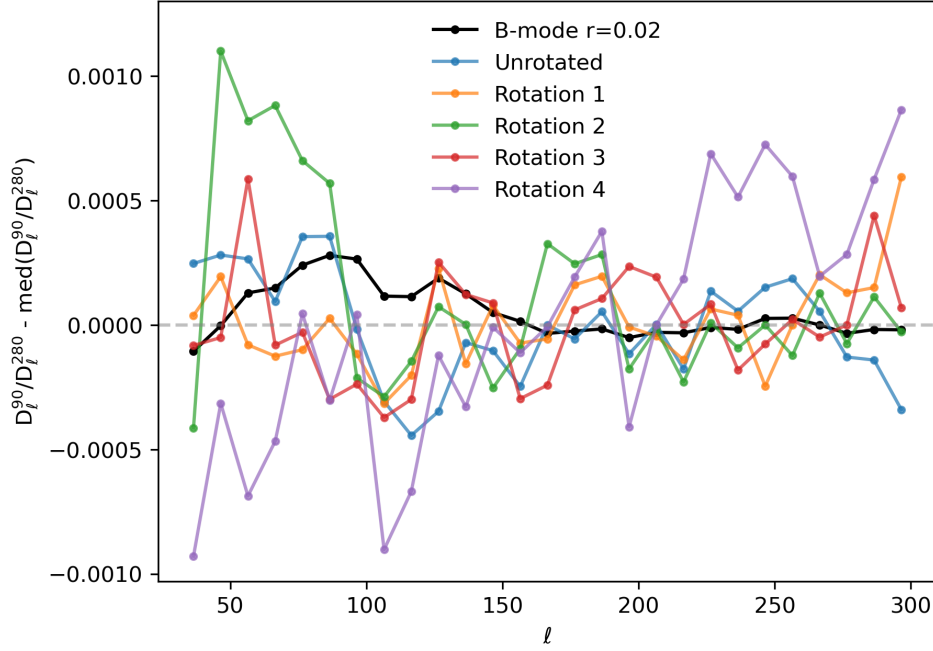


Figure 13. The ratios of the dust power spectra at 90 GHz to 280 GHz for the different β_d rotations, with the median across bandpower bins subtracted. Variations across multipole reflects an ℓ -dependent variation of the dust SED. The black curve shows the ratio of primordial B -mode power spectrum at $r = 0.02$ to the standard $\mathbf{d10}$ 280 GHz power spectrum. Rotations that induce a larger bias in r (e.g., Unrotated and Rotation 2) enhance the large-scale dust power at 90 GHz, mimicking tensor B -mode structure. This suggests that spatial features in β_d are responsible for the bias in r . The residual structure in the median subtracted dust power spectral ratio qualitatively corresponds to the excess large-scale power that the model absorbs as a larger—but incorrect— r signal.

A particularly relevant combination is $00 + 11 + 02$, which corresponds to the existing second-order moment extension modeling in [Azzoni et al. \(2021\)](#) that we adopt in this work. This captures the dominant behavior but begins to deviate from the full $\mathbf{d10}$ power spectrum (black dashed line). This discrepancy is particularly relevant at larger scales, where if the model underestimates dust power, a positive bias in r can be introduced as the pipeline compensates for the missing power. This deviation arises when either the level of frequency decorrelation is strong enough to induce high variance in $\delta\beta$, or the actual dust power spectrum deviates substantially from the assumed power-law form. Both effects are physically plausible, especially in realistic sky regions.

In these cases, the current moment-based model may become underconstrained. Including higher-order terms, in addition to the minimal moment expansion implemented in [Azzoni et al. \(2021\)](#), could better capture the observed behavior. Some examples can be found in [Mangilli et al. \(2021\)](#) and [Vacher et al. \(2022\)](#), where an extended moment expansion was applied in the contexts of Planck and *LiteBIRD* component separation, respectively. However, doing so comes at a cost: each added

term introduces additional parameters, which increases the uncertainty on r (i.e., inflates $\sigma(r)$).

Another source of bias lies in the neglected cross-correlations between moment terms. As shown in the bottom-right panel of Figure 14, the summed power of individual moment maps (orange line) differs from the power of their sum (blue line), indicating that cross-order correlations, especially between m_0 and m_1 , contribute significantly to the total signal. These correlations may become non-negligible under strong frequency decorrelation.

These results highlight the need to explore cross-order and higher-order moment-expansion terms for power spectral modeling. As power spectral degeneracies become more challenging at higher sensitivity, modeling frameworks that incorporate both harmonic space and pixel space information may offer robust solutions if the true sky has complex spectral index variation (e.g., [Remazeilles et al. 2021](#); [Azzoni et al. 2023](#); [Carones & Remazeilles 2024](#)). Importantly, such methods can enhance model fidelity without requiring additional nuisance parameters, thereby avoiding any potential degradation in $\sigma(r)$.

5. DISCUSSION

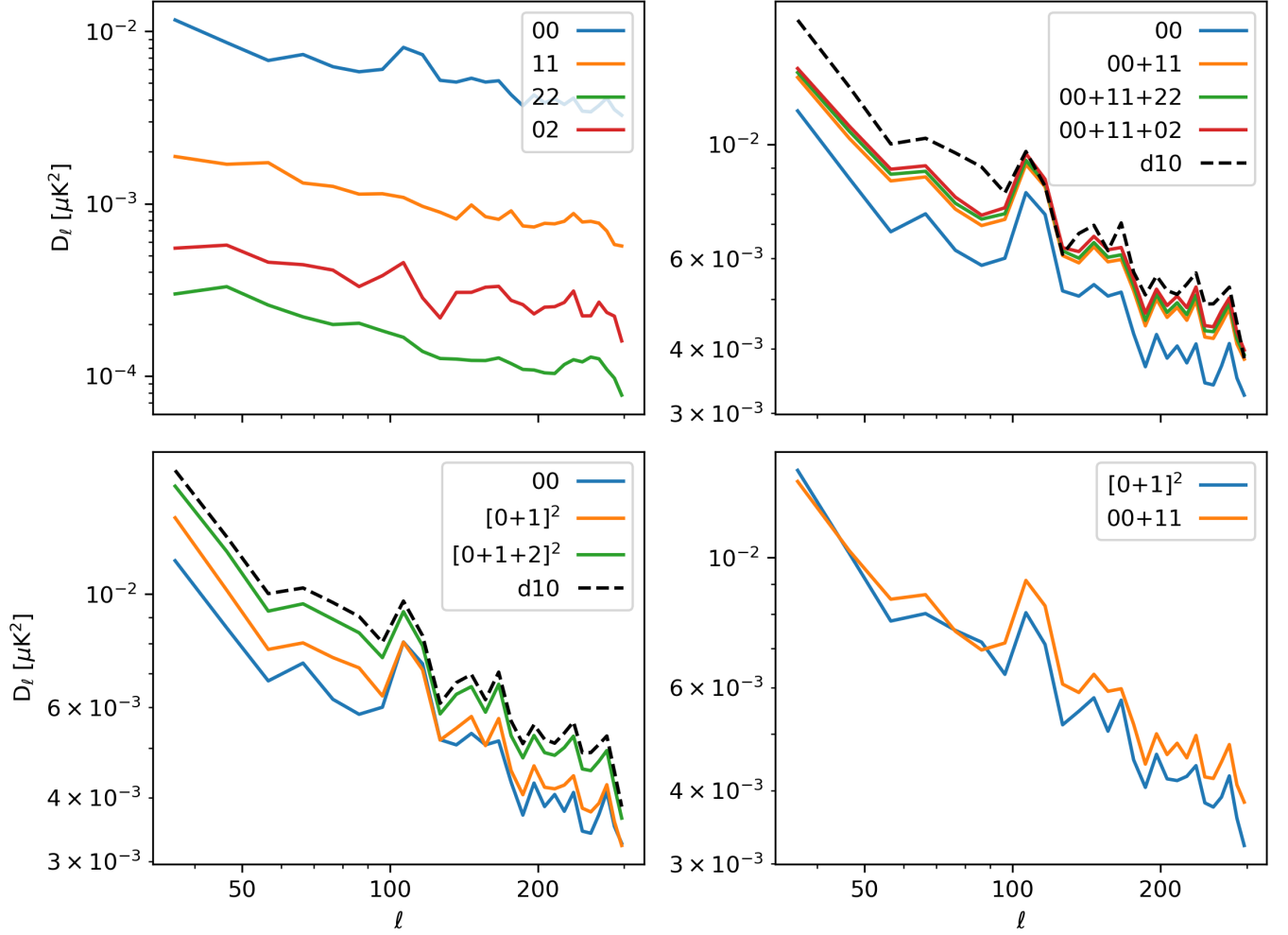


Figure 14. The 90 GHz power spectra of the leading-order moment maps in the β_d spatial scenario at $x_\beta = 1.6$. **Top Left:** auto-spectra and selected cross-spectra of moment maps, indicated with a pair of numbers (e.g., 00 means the auto spectra of the zeroth order moment map). **Top Right:** Selected combination of moment map auto-spectra and cross-spectra. The blue 00 spectrum is used in our fiducial pipeline and clearly underestimates the d10 spectrum (black). The red 00 + 11 + 02 is the combination used in the moment method we consider in this analysis; it also does not fully capture the d10 spectrum and explains why we see a biased result for r . **Bottom Left:** Selected power spectra for the sum of moment maps. We use square brackets to indicate power spectrum of map sums (e.g. $[0+1]^2$ means the power spectrum of the sum of zeroth and first order moment maps). The difference between the green line and black dashed line indicates the need for higher-order terms in this scenario where the dust is highly complex. **Bottom Right:** power spectra for the map sum and the sum of expansion power spectra to the first order. The difference between the two power spectrum shows the need to include the cross order term, 01, for accurate modeling.

In this work, we investigated the source of possible biases on the cosmological parameter r , arising from potential mismodeling of foreground spectral properties in component separation. Through a series of targeted simulations, including realistic spatially varying dust parameters and controlled covariance modeling, we identified conditions under which standard analysis pipelines can lead to biased r estimates or degraded fit quality.

We quantified dust complexity in terms of frequency decorrelation, controlled through variations in the dispersion of SED parameters. We found a clear trend: in-

creasing SED parameter dispersion leads to a stronger bias in r when modeled with a power spectrum approach, with variations in β_d having the largest effect. Section 2.3.1 noted that the anti-correlation between β_d and T_d templates can reduce the net decorrelation. Disentangling the origin of this anti-correlation is challenging for CMB experiments, as independently constraining T_d requires observations at higher frequencies typically in the THz range. In the absence of such information, it is difficult to determine whether the observed β_d - T_d

anti-correlation reflects physical dust properties or fitting degeneracies.

Focusing on β_d , we identified ℓ -dependent SED scaling as a primary driver of mismodeling that leads to a bias in r . Through moment-expansion analysis of dust maps, we showed that higher-order moment terms alter the power spectrum shape, particularly in lower frequency channels.

To assess the adequacy of power spectrum modeling, we evaluated the goodness-of-fit using χ^2 values. Models that assume a simple power-law angular power spectrum for foregrounds yield poor fits to the synchrotron simulations we considered. To improve fitting quality, modifications were needed in both the model definition and the covariance matrix. For foreground power spectra, adopting methods such as a per- ℓ fitting formalism may better account for deviations from a simple power law. For the data covariance, simulations should include both frequency decorrelation and an estimate of the ℓ -dependence of foreground power spectra to ensure a proper characterization of cross-channel correlations. Accurately determining the level of frequency decorrelation is challenging in practice, which complicates the generation of Gaussian simulations with appropriate decorrelation level for a simulation-based covariance. A practical approach is to first quantify the relationship between recovered moment amplitudes (B_d, B_s) and input decorrelation levels, begin with a simple Gaussian covariance, and iteratively introduce decorrelation effects based on the observed moment amplitude until convergence is achieved. Alternatively, an analytic solution to the data covariance could be used. These modifications will be important for accurately assessing the goodness-of-fit as power spectrum measurements become more precise.

Expanding the moment-expansion formalism to include cross-order and higher-order terms, as well as relaxing the assumption of a power-law β_d angular power spectrum, are promising directions for improving dust modeling accuracy, if needed by the data. However, such refinement must be balanced against the resulting increase in $\sigma(r)$. Future work could also explore the application of existing hybrid map- C_ℓ component separation approaches to these more complex foreground models. Ancillary datasets at other wavelengths may also be useful for constraining dust behavior and informing model selection.

In practice, we anticipate assessing the degree of complexity of the Simons Observatory data by checking the goodness of fit of the simplest models, and then increasing the complexity of the model to determine whether the estimate of r and the foreground parameters, and

the goodness of fit, changes when adding higher order terms. We would also expect to perform robustness tests to check the stability of our results derived from different subsets of the data (for example, excluding the 90 GHz or 150 GHz data, or using different regions of the sky), which could also reveal the need to enhance the model complexity. Implementing different foreground cleaning methods will continue to be valuable in assessing the consistency of results.

6. CONCLUSIONS

Our analysis highlights several key findings regarding the origin of foreground-induced biases in tensor-to-scalar ratio measurements. We summarize here the principal conclusions of our work.

1. Incorporating the effect of frequency decorrelation into the covariance matrix estimation was essential for achieving acceptable goodness of fit in the analyses presented here (see Figure 8). While beyond the scope of this work, full data-driven covariance estimation may be critical for future analyses on real data.
2. Spatial variations in β_d consistently lead to the strongest frequency decorrelation for a given scaling x_{β_d} (Figure 4) and the largest biases in the recovered tensor-to-scalar ratio r (Figure 9). For some of the higher values of the **d10** β_d scaling explored ($1.2 \leq x_{\beta_d} \leq 1.5$), the induced decorrelation remains within the range allowed by the physically-motivated **d12** model, yet produces a non-negligible bias in r . This trend is observed in both Gaussian and more realistic foreground simulations, underscoring β_d as the most influential parameter in driving frequency decorrelation and associated biases.
3. When isolating the contributions of dust amplitude and β_d (Figure 10), we find that the bias in r is strongly correlated with the choice of β_d , while the amplitude map has little impact. This confirms that it is the non-Gaussian structure of β_d , and potentially its coupling with the dust amplitude, that drives the residual r bias – especially in the high-dispersion regime where even the moment-expansion method fails to fully recover an unbiased estimate.
4. While other potential sources of bias, such as non-Gaussianity in the dust amplitude, limitations of the power-law spectral model, or lowest-order correlations between amplitude and β_d , cannot be fully excluded, they are unlikely to be dominant.

This is supported by (i) the equivalence in decorrelation between Gaussian and non-Gaussian β_d fields, (ii) the good PtE values obtained when using a power-law dust model, and (iii) explicit tests showing that low-order correlations between β_d and amplitude (Figure 6) have negligible impact on the bias in r (Figure 8). These results point to missing higher-order statistics in the current modeling framework as the most plausible origin of the residual bias.

5. The rotation analysis (Figure 11), in which the β_d map is rotated independently of the amplitude, reveals sensitivity to the spatial coupling between β_d and the dust amplitude. This supports the interpretation that a bias on r can arise from non-trivial correlations between these fields. Figure 13 further shows that different β_d maps yield distinct ℓ -dependence in the dust power spectrum, reinforcing the connection between the bias and changes in spectral shape across frequency.
6. While non-Gaussian amplitudes have a modest impact on r biases relative to Gaussian amplitudes with the same power spectrum, the non-Gaussianity of the β map has a significant effect. Figure 14 indicates that our current moment expansion (including the terms 00 + 11 + 02) underfits the decorrelation observed in the re-scaled d10 simulation (with $x_{\beta_d} = 1.6$), pointing to missing higher-order moment terms in the model. These terms include (i) the ones dependent on the β_d -amplitude correlations, and (ii) the moment terms of order higher than 2, which quantify non-Gaussianities of the β_d distribution (Vacher et al. 2024).

Future extensions of the analysis methods employed here could include higher-order terms in the expansion, which are straightforward to include in the current implementation of the moments method. Although this may increase parameter degeneracy and increase $\sigma(r)$, it would provide a more complete description of foreground complexity if the data require it. Alternative approaches could include incorporating the pixel-level correlations in the current model, as in the “hybrid” method proposed in Azzoni et al. (2023), or leverage moments-based frameworks operating in other domains beyond the power spectrum (e.g., Remazeilles et al. 2021; Carones & Remazeilles 2024). Improved measurements will enable sharper foreground characterization,

guiding the development of increasingly robust modeling techniques.

ACKNOWLEDGEMENTS

The authors would like to thank Irene Abril-Cabezas for useful feedback. This work was supported in part by a grant from the Simons Foundation (Award #457687, B.K.). The simulations presented in this article were performed on computational resources managed and supported by Princeton Research Computing. This work was carried out in part at the Jet Propulsion Laboratory, California Institute of Technology, under a contract with the National Aeronautics and Space Administration. DA acknowledges support from STFC under grant ST/W000903/1, and from the Beecroft Trust. CB acknowledges partial support by the Italian Space Agency *LiteBIRD* Project (ASI Grants No. 2020-9-HH.0 and 2016-24-H.1-2018), as well as the InDark and *LiteBIRD* Initiative of the National Institute for Nuclear Physics, and the Radio-ForegroundsPlus Project HORIZON-CL4-2023-SPACE-01, GA 101135036, and Project SPACE-IT-UP by the Italian Space Agency and Ministry of University and Research, Contract Number 2024-5-E.0. MLB acknowledges support from the UKRI/STFC (grant number ST/X006344/1). SEC acknowledges support from NSF grant No. AST-2441452, and from an Alfred P. Sloan Research Fellowship. JD acknowledges support from a Royal Society Wolfson Visiting Fellowship and from the Kavli Institute for Cosmology Cambridge and the Institute of Astronomy, Cambridge. NK acknowledges partial support from the InDark Initiative of the National Institute for Nuclear Physics (INFN), and the Radio-ForegroundsPlus Project HORIZON-CL4-2023-SPACE-01, GA 101135036, and Project SPACE-IT-UP by the Italian Space Agency and Ministry of University and Research, Contract Number 2024-5-E.0. MR acknowledges the support of the Spanish Ministry of Science and Innovation through grants PID2022-139223OB-C21 and PID2022-140670NA-I00, as well as the Radio-ForegroundsPlus Project HORIZON-CL4-2023-SPACE-01, GA 101135036. LV acknowledges partial support from the RadioForegroundsPlus Project HORIZON-CL4-2023-SPACE-01, GA 101135036. We acknowledge the use of *CAMB* (Lewis & Bridle 2002), *emcee* (Foreman-Mackey et al. 2013), *healpy* (Zonca et al. 2019), *matplotlib* (Hunter 2007), *numpy* (Harris et al. 2020), *PySM3* (Thorne et al. 2017; Zonca et al. 2021; The Pan-Experiment Galactic Science Group et al. 2025), and *scipy* (Virtanen et al. 2020) software packages.

REFERENCES

- Abazajian, K., Addison, G. E., Adshead, P., et al. 2022, *ApJ*, 926, 54, doi: [10.3847/1538-4357/ac1596](https://doi.org/10.3847/1538-4357/ac1596)
- Abitbol, M. H., Alonso, D., Simon, S. M., et al. 2021, *JCAP*, 2021, 032, doi: [10.1088/1475-7516/2021/05/032](https://doi.org/10.1088/1475-7516/2021/05/032)
- Abril-Cabezas, I., Hervías-Caimapo, C., von Hausegger, S., Sherwin, B. D., & Alonso, D. 2024, *MNRAS*, 527, 5751, doi: [10.1093/mnras/stad3529](https://doi.org/10.1093/mnras/stad3529)
- Ade, P., Aguirre, J., Ahmed, Z., et al. 2019, *JCAP*, 2019, 056, doi: [10.1088/1475-7516/2019/02/056](https://doi.org/10.1088/1475-7516/2019/02/056)
- Ade, P. A. R., Ahmed, Z., Amiri, M., et al. 2022, *ApJ*, 927, 77, doi: [10.3847/1538-4357/ac4886](https://doi.org/10.3847/1538-4357/ac4886)
- . 2023, *ApJ*, 945, 72, doi: [10.3847/1538-4357/acb64c](https://doi.org/10.3847/1538-4357/acb64c)
- Ade, P. A. R., Amiri, M., Benton, S. J., et al. 2025, *ApJ*, 978, 130, doi: [10.3847/1538-4357/ad900c](https://doi.org/10.3847/1538-4357/ad900c)
- Alonso, D., Sanchez, J., Slosar, A., & LSST Dark Energy Science Collaboration. 2019, *MNRAS*, 484, 4127, doi: [10.1093/mnras/stz093](https://doi.org/10.1093/mnras/stz093)
- Atkins, Z., Li, Z., Alonso, D., et al. 2024, arXiv e-prints, arXiv:2412.07068, doi: [10.48550/arXiv.2412.07068](https://doi.org/10.48550/arXiv.2412.07068)
- Azzoni, S., Abitbol, M. H., Alonso, D., et al. 2021, *Journal of Cosmology and Astroparticle Physics*, 2021, 047, doi: [10.1088/1475-7516/2021/05/047](https://doi.org/10.1088/1475-7516/2021/05/047)
- Azzoni, S., Alonso, D., Abitbol, M. H., Errard, J., & Krachmalnicoff, N. 2023, *JCAP*, 2023, 035, doi: [10.1088/1475-7516/2023/03/035](https://doi.org/10.1088/1475-7516/2023/03/035)
- BICEP/Keck Collaboration, Ade, P. A. R., Ahmed, Z., et al. 2016, *Phys. Rev. Lett.*, 116, 031302, doi: [10.1103/PhysRevLett.116.031302](https://doi.org/10.1103/PhysRevLett.116.031302)
- . 2021, *Physical Review Letters*, 127, 151301, doi: [10.1103/PhysRevLett.127.151301](https://doi.org/10.1103/PhysRevLett.127.151301)
- Carones, A., & Remazeilles, M. 2024, *JCAP*, 2024, 018, doi: [10.1088/1475-7516/2024/06/018](https://doi.org/10.1088/1475-7516/2024/06/018)
- Chluba, J., Hill, J. C., & Abitbol, M. H. 2017, *MNRAS*, 472, 1195, doi: [10.1093/mnras/stx1982](https://doi.org/10.1093/mnras/stx1982)
- Choi, S. K., & Page, L. A. 2015, *JCAP*, 2015, 020, doi: [10.1088/1475-7516/2015/12/020](https://doi.org/10.1088/1475-7516/2015/12/020)
- Demyk, K., Meny, C., Lu, X. H., et al. 2017, *A&A*, 600, A123, doi: [10.1051/0004-6361/201629711](https://doi.org/10.1051/0004-6361/201629711)
- Foreman-Mackey, D., Hogg, D. W., Lang, D., & Goodman, J. 2013, *PASP*, 125, 306, doi: [10.1086/670067](https://doi.org/10.1086/670067)
- Guth, A. H. 1981, *Physical Review D*, 23, 347, doi: [10.1103/PhysRevD.23.347](https://doi.org/10.1103/PhysRevD.23.347)
- Górski, K. M., Hivon, E., Banday, A. J., et al. 2005, *The Astrophysical Journal*, 622, 759, doi: [10.1086/427976](https://doi.org/10.1086/427976)
- Hamimeche, S., & Lewis, A. 2008, *PhRvD*, 77, 103013, doi: [10.1103/PhysRevD.77.103013](https://doi.org/10.1103/PhysRevD.77.103013)
- Harris, C. R., Millman, K. J., van der Walt, S. J., et al. 2020, *Nature*, 585, 357, doi: [10.1038/s41586-020-2649-2](https://doi.org/10.1038/s41586-020-2649-2)
- Hervías-Caimapo, C., & Hufenberger, K. M. 2022, *ApJ*, 928, 65, doi: [10.3847/1538-4357/ac54b2](https://doi.org/10.3847/1538-4357/ac54b2)
- Hervías-Caimapo, C., Wolz, K., La Posta, A., et al. 2025, *JCAP*, 2025, 055, doi: [10.1088/1475-7516/2025/06/055](https://doi.org/10.1088/1475-7516/2025/06/055)
- Hinshaw, G., Nolta, M. R., Bennett, C. L., et al. 2007, *ApJS*, 170, 288, doi: [10.1086/513698](https://doi.org/10.1086/513698)
- Hunter, J. D. 2007, *Computing in Science and Engineering*, 9, 90, doi: [10.1109/MCSE.2007.55](https://doi.org/10.1109/MCSE.2007.55)
- Kamionkowski, M., Kosowsky, A., & Stebbins, A. 1997, *Physical Review Letters*, 78, 2058, doi: [10.1103/PhysRevLett.78.2058](https://doi.org/10.1103/PhysRevLett.78.2058)
- Knox, L. 1995, *PhRvD*, 52, 4307, doi: [10.1103/PhysRevD.52.4307](https://doi.org/10.1103/PhysRevD.52.4307)
- Krachmalnicoff, N., Carretti, E., Baccigalupi, C., et al. 2018, *A&A*, 618, A166, doi: [10.1051/0004-6361/201832768](https://doi.org/10.1051/0004-6361/201832768)
- Lewis, A., & Bridle, S. 2002, *PhRvD*, 66, 103511, doi: [10.1103/PhysRevD.66.103511](https://doi.org/10.1103/PhysRevD.66.103511)
- Lewis, A., & Challinor, A. 2006, *Weak Gravitational Lensing of the CMB*, doi: [10.1016/j.physrep.2006.03.002](https://doi.org/10.1016/j.physrep.2006.03.002)
- Lewis, A., Challinor, A., & Turok, N. 2001, *Phys. Rev. D*, 65, 023505, doi: [10.1103/PhysRevD.65.023505](https://doi.org/10.1103/PhysRevD.65.023505)
- Linde, A. D. 1982, *Physics Letters B*, 108, 389, doi: [10.1016/0370-2693\(82\)91219-9](https://doi.org/10.1016/0370-2693(82)91219-9)
- LiteBIRD Collaboration, Allys, E., Arnold, K., et al. 2023, *Progress of Theoretical and Experimental Physics*, 2023, 042F01, doi: [10.1093/ptep/ptac150](https://doi.org/10.1093/ptep/ptac150)
- Mangilli, A., Aumont, J., Rotti, A., et al. 2021, *A&A*, 647, A52, doi: [10.1051/0004-6361/201937367](https://doi.org/10.1051/0004-6361/201937367)
- Martínez-Solaeche, G., Karakci, A., & Delabrouille, J. 2018, *MNRAS*, 476, 1310, doi: [10.1093/mnras/sty204](https://doi.org/10.1093/mnras/sty204)
- Miville-Deschênes, M. A., Ysard, N., Lavabre, A., et al. 2008, *A&A*, 490, 1093, doi: [10.1051/0004-6361:200809484](https://doi.org/10.1051/0004-6361:200809484)
- Pelgrims, V., Clark, S. E., Hensley, B. S., et al. 2021, *A&A*, 647, A16, doi: [10.1051/0004-6361/202040218](https://doi.org/10.1051/0004-6361/202040218)
- Planck Collaboration, Ade, P. A. R., Aghanim, N., et al. 2014, *A&A*, 571, A15, doi: [10.1051/0004-6361/201321573](https://doi.org/10.1051/0004-6361/201321573)
- Planck Collaboration, Adam, R., Ade, P. A. R., et al. 2016a, *A&A*, 586, A133, doi: [10.1051/0004-6361/201425034](https://doi.org/10.1051/0004-6361/201425034)
- Planck Collaboration, Aghanim, N., Arnaud, M., et al. 2016b, *Astronomy & Astrophysics*, 594, A11, doi: [10.1051/0004-6361/201526926](https://doi.org/10.1051/0004-6361/201526926)
- Planck Collaboration, Aghanim, N., Ashdown, M., et al. 2016c, *A&A*, 596, A109, doi: [10.1051/0004-6361/201629022](https://doi.org/10.1051/0004-6361/201629022)
- . 2017, *A&A*, 599, A51, doi: [10.1051/0004-6361/201629164](https://doi.org/10.1051/0004-6361/201629164)
- Planck Collaboration, Akrami, Y., Ashdown, M., et al. 2020a, *Astronomy & Astrophysics*, 641, A11, doi: [10.1051/0004-6361/201832618](https://doi.org/10.1051/0004-6361/201832618)

- Planck Collaboration, Aghanim, N., Akrami, Y., et al. 2020b, *A&A*, 641, A6, doi: [10.1051/0004-6361/201833910](https://doi.org/10.1051/0004-6361/201833910)
- Planck Collaboration, Akrami, Y., Ashdown, M., et al. 2020c, *A&A*, 641, A4, doi: [10.1051/0004-6361/201833881](https://doi.org/10.1051/0004-6361/201833881)
- Planck Collaboration, Akrami, Y., Andersen, K. J., et al. 2020d, *A&A*, 643, A42, doi: [10.1051/0004-6361/202038073](https://doi.org/10.1051/0004-6361/202038073)
- Remazeilles, M., Delabrouille, J., & Cardoso, J.-F. 2011, *MNRAS*, 418, 467, doi: [10.1111/j.1365-2966.2011.19497.x](https://doi.org/10.1111/j.1365-2966.2011.19497.x)
- Remazeilles, M., Dickinson, C., Banday, A. J., Bigot-Sazy, M. A., & Ghosh, T. 2015, *MNRAS*, 451, 4311, doi: [10.1093/mnras/stv1274](https://doi.org/10.1093/mnras/stv1274)
- Remazeilles, M., Dickinson, C., Eriksen, H. K. K., & Wehus, I. K. 2016, *MNRAS*, 458, 2032, doi: [10.1093/mnras/stw441](https://doi.org/10.1093/mnras/stw441)
- Remazeilles, M., Rotti, A., & Chluba, J. 2021, *MNRAS*, 503, 2478, doi: [10.1093/mnras/stab648](https://doi.org/10.1093/mnras/stab648)
- Ritacco, A., Boulanger, F., Guillet, V., et al. 2023, *A&A*, 670, A163, doi: [10.1051/0004-6361/202244269](https://doi.org/10.1051/0004-6361/202244269)
- Seljak, U., & Zaldarriaga, M. 1997, *Physical Review Letters*, 78, 2054, doi: [10.1103/PhysRevLett.78.2054](https://doi.org/10.1103/PhysRevLett.78.2054)
- Shetty, R., Kauffmann, J., Schnee, S., Goodman, A. A., & Ercolano, B. 2009, *ApJ*, 696, 2234, doi: [10.1088/0004-637X/696/2/2234](https://doi.org/10.1088/0004-637X/696/2/2234)
- Tassis, K., & Pavlidou, V. 2015, *MNRAS*, 451, L90, doi: [10.1093/mnrasl/slv077](https://doi.org/10.1093/mnrasl/slv077)
- The Pan-Experiment Galactic Science Group, Borrill, J., Clark, S. E., et al. 2025, arXiv e-prints, arXiv:2502.20452, doi: [10.48550/arXiv.2502.20452](https://doi.org/10.48550/arXiv.2502.20452)
- Thorne, B., Dunkley, J., Alonso, D., & Naess, S. 2017, *MNRAS*, 469, 2821, doi: [10.1093/mnras/stx949](https://doi.org/10.1093/mnras/stx949)
- Tristram, M., Banday, A. J., Górski, K. M., et al. 2022, *PhRvD*, 105, 083524, doi: [10.1103/PhysRevD.105.083524](https://doi.org/10.1103/PhysRevD.105.083524)
- Vacher, L., Aumont, J., Boulanger, F., et al. 2023a, *A&A*, 672, A146, doi: [10.1051/0004-6361/202245292](https://doi.org/10.1051/0004-6361/202245292)
- Vacher, L., Aumont, J., Montier, L., et al. 2022, *A&A*, 660, A111, doi: [10.1051/0004-6361/202142664](https://doi.org/10.1051/0004-6361/202142664)
- Vacher, L., Carones, A., Aumont, J., et al. 2024, arXiv e-prints, arXiv:2411.11649, doi: [10.48550/arXiv.2411.11649](https://doi.org/10.48550/arXiv.2411.11649)
- Vacher, L., Chluba, J., Aumont, J., Rotti, A., & Montier, L. 2023b, *A&A*, 669, A5, doi: [10.1051/0004-6361/202243913](https://doi.org/10.1051/0004-6361/202243913)
- Virtanen, P., Gommers, R., Oliphant, T. E., et al. 2020, *Nature Methods*, 17, 261, doi: [10.1038/s41592-019-0686-2](https://doi.org/10.1038/s41592-019-0686-2)
- Wolz, K., Azzoni, S., Hervías-Caimapo, C., et al. 2024, *A&A*, 686, A16, doi: [10.1051/0004-6361/202346105](https://doi.org/10.1051/0004-6361/202346105)
- Zaldarriaga, M., & Seljak, U. c. v. 1998, *Phys. Rev. D*, 58, 023003, doi: [10.1103/PhysRevD.58.023003](https://doi.org/10.1103/PhysRevD.58.023003)
- Zonca, A., Singer, L., Lenz, D., et al. 2019, *The Journal of Open Source Software*, 4, 1298, doi: [10.21105/joss.01298](https://doi.org/10.21105/joss.01298)
- Zonca, A., Thorne, B., Krachmalnicoff, N., & Borrill, J. 2021, *The Journal of Open Source Software*, 6, 3783, doi: [10.21105/joss.03783](https://doi.org/10.21105/joss.03783)